Computers and Geotechnics 196 (2026) 108163

Contents lists available at ScienceDirect

Computers and Geotechnics

journal homepage: www.elsevier.com/locate/compgeo

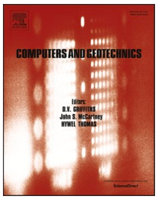

A novel coupled MPM-SDEM framework for simulating non-spherical objects in flow-type landslide

Jun Fang [a], Wei Ji [a,*], Tianju Xue [b], Yu Wang [b], Jidong Zhao [b], Yupeng Jiang [c], Clarence Edward Choi [a,*]

[a] *Department of Civil Engineering, The University of Hong Kong, HKSAR, Hong Kong, China*
[b] *Department of Civil and Environmental Engineering, The Hong Kong University of Science and Technology, HKSAR, Hong Kong, China*
[c] *Institut für Baumechanik und Numerische Mechanik, Leibniz Universität Hannover, Welfengarten 1 30167, Hannover, Germany*

ARTICLE INFO

Keywords:
MPM-SDEM
Non-sphericalparticle
Flow-block interaction
Travelling distance
Impact force

ABSTRACT

Objects such as cars and shelters are often transported and buried by flow-type landslides, including granular flows and debris avalanches. To predict the travelling distance and buried location of these non-spherical objects, this study develops a coupled MPM-SDEM framework that integrates a sphero-polyhedron DEM for object modelling with the material point method for flow-type landslides. Validations against theoretical and experimental benchmarks confirm its robustness in predicting object travelling distance and impact force. A comparison between MPM-SDEM and MPM-LSDEM demonstrates that MPM-SDEM outperforms MPM-LSDEM, with efficiency improved by 97% and accuracy enhanced by 63%. A parametric study using the calibrated MPM-SDEM solver is conducted to investigate the effects of the initial column height and the block-to-column distance. Simulation results reveal the positive dependence of maximum impact force, normalized by static force, on the Froude number. A modified Froude number is proposed that incorporates the block-to-column distance as the macroscopic characteristic scale instead of flow depth, significantly enhancing displacement predictions. The MPM-SDEM framework offers an efficient and robust tool for flow-structure simulations, with strong potential for search and rescue applications.

1. Introduction

The Intergovernmental Panel on Climate Change reported that the number of rainfall-induced landslides is expected to increase owing to climate change. Among these landslide types, the flow-type ones, which transport large volumes of sediments downslope under the influence of gravity, are the most dangerous. One of the most significant hazards posed by flow-type landslides is when they displace and bury objects with victims trapped inside. Displaced objects from their original locations make rescue efforts considerably more challenging. In the Shuicheng, China, in 2009, sediments displaced objects by up to 500 m downstream from their original locations (Zhao et al., 2020). Further compounding the challenges of search and rescue, sediment deposits can cover massive areas. For example, the debris from the 2016 Guinsaugon, Philippines, event covered an area 1.52 km by 4.1 km (Lagmay et al., 2008). Even with ground penetration radar and canine units, with limited detection depths, search and rescue operations were ineffective without clear search areas to focus on. It is often reported after a landslide that given the scale and lack of information (e.g., subsurface soil properties and conditions), rescue efforts are wasted during the most critical first few days. For example, rescuers tragically wasted the first six days excavating in the wrong location in Guinsaugon, Philippines, in 2006, because the entire village was displaced 600 m downstream. Evidently, the existing understanding of the transport and burial mechanisms of objects is extremely limited.

To simulate the transport of objects by flowing sediments, different numerical solvers have been used. Current numerical approaches for flow-structure interaction can be broadly divided into discrete method (e.g. Discrete element method (DEM), Salciarini et al., 2010; Zhao et al., 2017), particle-based continuum methods (e.g., Smoothed Particle Hydrodynamics (SPH), Dai et al., 2017; Zhang et al., 2024; Material Point Method (MPM), Liang et al., 2023; Liu et al., 2024), and hybrid methods (e.g., Trujillo-Vela et al., 2020; Ren et al., 2022; Shi et al., 2024). Discrete methods explicitly track individual particles and resolve their contact interactions (Wang et al., 2025). For example, DEM has been applied to study flow-type landslide-block interactions by adjusting the

---

* Corresponding authors.
E-mail addresses: gvhk@connect.hku.hkgvhk (W. Ji), cechoi@hku.hk (C.E. Choi).

https://doi.org/10.1016/j.compgeo.2026.108163
Received 21 November 2025; Received in revised form 31 March 2026; Accepted 13 April 2026

particle size of the discrete elements (Su et al., 2019 & 2021). However, the need to track every particle makes DEM computationally expensive, particularly for large-scale systems involving millions of particles (Donev et al., 2005; Feng et al., 2014).

In contrast, particle-based continuum methods exhibit better computational performance for simulating flow material (Augarde et al., 2021; Wang et al., 2025; Kim et al., 2025; Troncone et al., 2025). The continuum models treat the material as a continuous medium, described by averaged properties (e.g., density, velocity, stress) using partial differential equations, such as the Navier-Stokes equations for fluids or elastoplastic constitutive equations for solids (Liang et al., 2023). Instead of tracking individual particles, continuum methods solve for field variables over a discretized grid (de Vaucorbeil et al., 2020). Nevertheless, the inherent grid dependence of continuum models imposes certain limitations. For example, Liu et al. (2018) used the MPM to simulate sand flow impacting a non-spherical block, where both the sand flow and the block were modelled within the MPM framework. In MPM approach, momentum exchange is conducted on a fixed Eulerian background grid, which remains unchanged in size and position over time. Without both explicit surface contact representation and native support for rigid kinematics, this method struggles to prevent interpenetration reliably and to handle stiffness contrasts in rigid blocks, thereby making accurate enforcement of rigid body constraints and rotational motion capture challenging (Acosta et al., 2021; Bird et al., 2025).

To combine the strengths of continuum and discrete approaches, hybrid methods have been developed (Liang et al., 2023; Jiang et al., 2022), whereby incoming flowing sediments are modelled using the continuum method, while non-spherical blocks are represented with discrete techniques. Usually, a sphere-cluster method (Sveinsson et al., 2020; Shi et al., 2024) refers to a rigid assembly of spherical particles to approximate block-shaped particles, also known as a clump. Although the sphere-cluster method has been widely used in the DEM model, there are two limitations: (1) It typically requires a large number of subparticles to accurately represent non-spherical shapes, substantially increasing particle number and thus computational cost for field-scale simulations (Giannis et al., 2023); (2) It can introduce errors in temporal changes of contact forces, particle interlocking, and shear behavior, especially in multi-contact scenarios (Berry et al., 2023). An alternative is the node-to-surface approach, which discretizes the surface of each particle into a set of nodes. This technique has been successfully implemented in the level-set-based DEM (LSDEM) method to capture arbitrary surface geometries (Zhao et al., 2023; Choi, 2024). However, the heavy reliance of LSDEM on nodes reduces its efficiency in simulating multi-block systems. In contrast, the mesh-based Spheropolyhedron Discrete Element Method (SDEM) strikes an optimal balance between accuracy and computational efficiency (Jiang et al., 2020; Ren et al., 2022). Unlike the sphere-cluster and node-to-surface approaches, SDEM represents non-spherical particles using sphero-polyhedron, where edges of geometric features are smoothed via Minkowski sum with spheres in three dimensions (Zhao et al., 2023; Galindo-Torres, 2013). This method efficiently eliminates sharp-corner singularities by transforming singular vertex-edge-face contacts into smooth, continuous primitive interactions. As a result, force discontinuities, particle locking, and numerical instabilities are avoided (Galindo-Torres, 2013; Höhner et al., 2014). Additionally, mesh-based sphero-polyhedron has the potential to achieve close geometric approximation by the controlled dilation of surface triangulation, accurately capturing concave features and sharp edges without the surface bumps or volume errors typical of multi-sphere approximations (Galindo-Torres & Pedroso, 2010; Wang et al., 2025). Furthermore, SDEM is well-suited for robust coupling with continuum solvers, such as the Material Point Method (MPM), thereby providing a powerful platform for multi-scale simulations (Ren et al., 2022).

In this study, we develop an MPM-SDEM method to achieve a reliable balance of geometric accuracy, contact stability, and computational efficiency for modeling the dynamic impact of flow-type landslide on non-spherical objects. The proposed solver is validated by a theoretical solution and two physical experiments. In addition, the proposed solver is compared with the existing MPM-LSDEM method. Finally, the well-calibrated MPM-SDEM is applied to provide insights into the transport and burial mechanisms of non-spherical objects from flow-type landslides.

2. Coupled MPM-SDEM Methodology

We conduct the numerical simulations by developing an MPM-SDEM framework here. It can reproduce the flow-type landslide down an inclined channel impacting the block by treating the continuous fluid and discrete particles with MPM and SDEM, respectively. The motions of particles in SDEM are assumed to be governed by Newton's equations and the continuous material in MPM is described by the momentum equations. The interaction between flow-type landslide and object is achieved by exchanging contact force information at every timestep.

2.1. Governing equations for the particles in MPM

In MPM, the material is discretized into Lagrangian particles, which are also called material point (MP), carrying key properties such as mass, velocity, position, and deformation information (de Vaucorbeil et al., 2020). These material points move through a fixed Eulerian background grid, which serves as a computational framework for solving momentum equations, as follows:

$$\rho\frac{D\boldsymbol{v}}{Dt} = \nabla \bullet \boldsymbol{\sigma} + \rho\boldsymbol{g} + \boldsymbol{f}_{\mathrm{c}} \tag{1}$$

where ρ is the bulk density, $\boldsymbol{v}$ is the velocity vector, $\boldsymbol{\sigma}$ is the Cauchy stress tensor, and $\boldsymbol{g}$ is the gravity vector. $\boldsymbol{f}_{\mathrm{c}}$ is the volume-averaged force density, which is derived from contact force between MPM and SDEM. The Dirichlet boundary condition is used here, as detailed in Appendix A.

As shown in Fig. 1, the MPM procedure in each time step consists of four key stages. First (Fig. 1a), the kinematics of the MPs, including mass, momentum and stress, are extrapolated to the nodes utilizing quadratic B splines (Jiang et al., 2016), which is often called as particle-to-grid mapping (P2G). The quadratic B spline is defined as:

$$w(x) = \begin{cases} \frac{3}{4} - |x|^2 0 \leq |x| < \frac{1}{2} \\ \frac{1}{2}\left(\frac{3}{2} - |x|\right)^2 \frac{1}{2} \leq |x| < \frac{3}{2} \\ 0 \frac{3}{2} \leq |x| \end{cases} \tag{2}$$

The next stage (Fig. 1b), the node momentum is updated through an explicit time integration, as follows:

$$m_{\mathrm{Ij}}\boldsymbol{v}_{\mathrm{Ij}})^{t+1} = \Delta t\boldsymbol{f}_{\mathrm{Ij}} \tag{3}$$

where the subscript I means variable on background node, and j is the j th node, m_{Ij} is mass, Δt is timestep, and $\boldsymbol{f}_{\mathrm{Ij}}$ is force on node, which includes internal particle force, coupling force, and gravity.

Following the G2G stage, updated node quantities in the grid are then mapped back to MPs, referred to as grid-to-particle mapping (G2P) stage (Fig. 1c). In the third computational step, the updated variables include stress tensor, velocity, and deformation gradient.

The stress tensor σ is calculated using a constitutive model to capture flow phase transition. Following Dunatunga & Kamrin (2015), a hyperelastic-plastic constitutive model with gasification treatment is adopted. When intense shearing triggers volumetric expansion and particle contacts are largely lost, the material is developed into the gasified regime (Faug 2015), where the smooth transition between

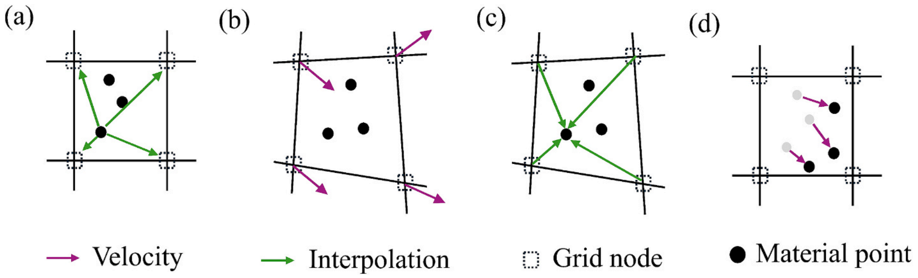

Fig. 1. The procedure of MPM: (a) particle-to-grid mapping (P2G); (b) grid-to-grid mapping (G2G); (c) grid-to-particle mapping (G2P); (d) particle-to-particle mapping (P2P).

dense and dilute states is captured using the *trans*-phase constitutive framework proposed by Dunatunga & Kamrin (2015). In the gasified regime, where ρ is smaller than a critical threshold ρ_c, a stress-free regime is assumed and stress σ is considered as zero. This assumption has been demonstrated and used for column collapse (Dunatunga and Kamrin, 2015). In this study, ρ_c is assumed to be the initial density of material point (Dunatunga & Kamrin, 2015). In contrast, when $\rho \geq \rho_c$, the flow material would be treated as a continuum body. The Drucker-Prager yield criterion is employed to distinguish between hyperelastic and plastic states (Dunatunga and Kamrin 2015). More details can be found in Appendix B.

In the last stage (Fig. 1d), the MPs are updated with respect to their position and state variables, which is usually referred to as the particle-to-particle mapping (P2P). At this stage, the particle velocity is updated based on node velocities. Here the combination of the fluid-implicit-particle (FLIP) method and the particle-in-cell (PIC) method has been adopted by introducing the blending ratio of FLIP and PIC, $\alpha \in [0, 1]$ (Stomakhin et al., 2013). The formulation for velocity update scheme for material point is given as follows:

$$\boldsymbol{v}_{\mathrm{p}}^{n+1} = \alpha\left(\boldsymbol{v}_{\mathrm{p}}^{n} + \frac{\sum_{i=1}^{N_I} w_{\mathrm{Ii}}\left(\boldsymbol{X}_{\mathrm{pj}}\right)\Delta t \boldsymbol{f}_{\mathrm{Ij}}}{m_{\mathrm{i}}}\right) + (1-\alpha)\sum_{i=1}^{N_I} w_{\mathrm{Ii}}\left(\boldsymbol{X}_{\mathrm{pj}}\right)\overline{\boldsymbol{v}}_{\mathrm{Ii}} \tag{4}$$

where $\overline{\boldsymbol{v}}_{\mathrm{Ii}}$ is the i th nodal velocity.

The FLIP–PIC blending ratio controls the trade-off between energy dissipation and stability, which has been extensively examined (Jiang et al., 2022; Blatny et al., 2025). FLIP has much less energy dissipation than PIC but is more unstable. A small PIC blending (1%-5%, i.e., $\alpha = 0.95$–0.99) significantly enhances stability without notably affecting impact forces or deposition patterns. However, when the blending of PIC is larger than 10% (i.e., $\alpha < 0.9$), increased dissipation can reduce peak velocity by 10%-15%. The most common scheme in MPM is FLIP (with a little blending with PIC for stability) for the velocity update. Blatny et al. (2025) reported that $\alpha = 0.99$ provides optimal balance, reducing pressure oscillations and improving particle distribution uniformity while preserving stress–strain convergence and bulk modulus accuracy. Based on these findings, we adopt $\alpha = 0.99$ in this study.

2.2. Governing equations for the blocks in SDEM

The sphero-polyhedron DEM is capable of representing a wide range of particle shapes, and is used here to reproduce the non-spherical particle. A sphero-polygon is defined as the Minkowski sum of a polyhedron to represent the irregular shape of near-rigid object and a sphere of radius R, which forms an elastic layer to calculate the contact forces among particles. Taking a sphero-cube particle as an example, as illustrated in Fig. 2, the generation process involves two steps: (1) Initially cube P with side length h_b is shrunk by a distance equal to the sphere radius, R, resulting in a smaller cube S with side length of $h_b - 2R$; and (2) The shrunken cubic is then dilated by using the same sphere, which is equivalent to positioning the center of the hemisphere in close conformance with the surface of the eroded cube, thereby achieving comprehensive coverage. The cube ends up having rounded corners and edges. In this framework, the spheropolyhedral representation is derived from Minkowski summation of a polyhedron and sphere. This representation streamlines contact detection by reducing interactions to efficient distance computations between skeletal polyhedra, adjusted for the sweeping radius. This mitigates numerical challenges associated with sharp edges, including contact multiplicity and instability, while enabling simulations of complex particle shapes with reduced computational overhead.

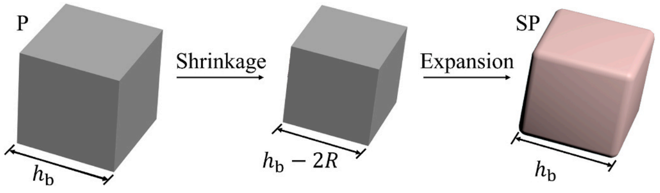

Fig. 2. Schematic diagram showing shrinkage and expansion procedures for a typical sphero-cube.

It is assumed that the translational and rotational motions of SDEM particle are solved by Newton's second law, which can be written as:

$$m_{\mathrm{Pi}}\frac{d\boldsymbol{v}_{\mathrm{Pi}}}{dt} = \sum_{j=1}^{n_{\mathrm{i}}}\boldsymbol{F}_{\mathrm{ij}} + \boldsymbol{F}_{\mathrm{g}} + \sum_{p=1}^{n_{\mathrm{p}}}\boldsymbol{F}_{\mathrm{c,\,p}} \tag{5}$$

$$I_{\mathrm{Pi}}\frac{d\boldsymbol{w}_{\mathrm{Pi}}}{dt} = \sum_{j=1}^{n_{\mathrm{i}}}\boldsymbol{M}_{\mathrm{ij}} + \boldsymbol{M}_{\mathrm{c}} \tag{6}$$

where m_{Pi} and I_{Pi} are the mass and moment of inertial of a single SDEM particle i, respectively. $\boldsymbol{v}_{\mathrm{Pi}}$ and $\boldsymbol{w}_{\mathrm{Pi}}$ are the translational and rotational velocity of particle i, respectively. n_{i} is the total contact number of SDEM particle for particle i. $\boldsymbol{M}_{\mathrm{ij}}$ and $\boldsymbol{M}_{\mathrm{c}}$ is the resistant moments acting on particle i by particle j and by MPs, respectively. $\boldsymbol{F}_{\mathrm{ij}}$ is the contact force on particle i by particle j. $\boldsymbol{F}_{\mathrm{g}}$ is the gravitational force. $\boldsymbol{F}_{\mathrm{c,\,p}}$ is the contact force on particle i by p-th MP. n_{p} is the total contact number of MP for particle i.

An important advantage of the sphero-polyhedron technique is its ability to enable a straightforward and efficient definition of contact laws between particles, which is accomplished by smoothing the edges of all geometric features with spheres in three dimensions. To simulate the contact between two sphero-polyhedron particles, each particle is decomposed into a set of geometric features, including edges, faces and vertices. Fig. 3 shows the possible contacts that are considered in the method between vertex and face, edge and edge, and vertex and edge. Based on these definitions, the face-face and face-edge interactions are not needed (Galindo-Torres, 2013). This is because that edge-face contact is equivalently treated as the face interacting with the two endpoints of the edge, and the face-face contact is represented as a face interacting with the vertices of the opposing face (Neto et al., 2022) These equivalent treatments ensure conservation of the net contact forces and

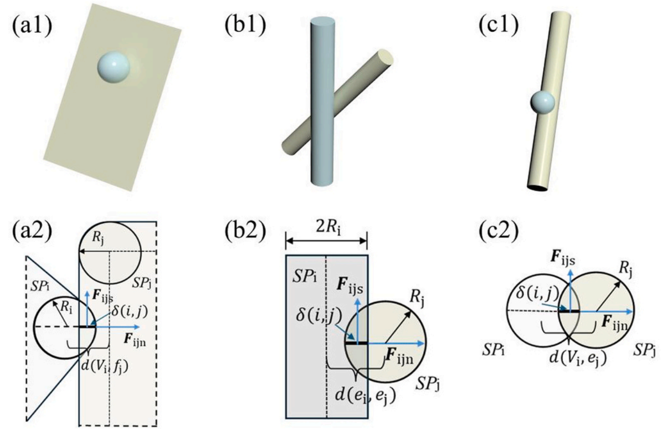

Fig. 3. The potential contacts between two sphero-polyhedron particles: (a1-a2) vertex-face contact; (b1-b2) edge-edge contact; (c1-c2) vertex-edge contact (*SP*: Sphero-polyhedron particle; *R*: Sphere radius in SDEM; *d*: distance between two particles; $\delta(i,j)$: overlapping between SDEM particle *i* and SDEM particle *j*; $\boldsymbol{F}_{ij}$: contact force between SDEM particle *i* and SDEM particle *j*, where *n* is normal force and *s* is shear force).

moments, thereby preserving the mechanical response identical to that derived from explicit edge-face or face-face contact algorithms. This strategy improves computational efficiency by reducing the number of distinct contact modes.

To determine whether the contact between sphero-polyhedron *i* and sphero-polyhedron *j* is built, a distance function $d(V_i, f_j)$ must be defined to calculate the overlapping distance $\delta(i,j)$ (Fig. 3). The distance between two vertices is calculated as the distance between two points in three-dimensional space. The distance between vertex and an edge is determined as the distance from the vertex to the point where a ray, passing through the vertex and perpendicular to the edge, intersects the edge. And the distance between a vertex and a face is the distance from the vertex to a point on the face connected by a line perpendicular to the plane of a face. The overlapping distance $\delta(i,j)$ can be calculated as follows:

$$\delta(\mathrm{i},\mathrm{j}) = \mathrm{R_i} + \mathrm{R_j} - \mathrm{d}(\mathrm{V_i}, \mathrm{f_j}) \tag{7}$$

where $d(V_i, f_j)$ is the Euclidean distance between particles *i* and *j*. R_i and R_j are the radius of spheres used to shrink and expand sphero-polyhedron *i* and sphero-polyhedron *j*, respectively. Since both sphero-polyhedron *i* and sphero-polyhedron *j* are expanded by spheres with radii of R_i and R_j, respectively, there is complete contact when the distance between *i* and *j* is less than the sum of R_i and R_j, where $\delta(i,j) > 0$.

Thereafter, the contact force can be calculated following the contact law in the conventional DEM code (Zhou et al., 2019; Descantes et al., 2019; Qu et al., 2019). The normal elastic force $\mathbf{F}_{ij}^{n}$ is calculated based on Hooke's law and the shear force $\mathbf{F}_{ij}^{s}$ is determined based on Coulomb friction law (Ren et al., 2022), as following:

$$\mathbf{F}_{ij}^{n} = K_n\,\delta(i,j) \tag{8}$$

$$\mathbf{F}_{ij}^{s} = \min\{\mu_b \mathbf{F}_{ij}^{n}, -K_t\xi - c_t v_t\} \tag{9}$$

where ξ the cumulative tangential displacement before sliding occurs. v_t is the tangential relative velocity, c_t is the damping coefficient. K_n and K_t are the normal contact stiffness and tangent contact stiffness, respectively, expressed by the equation (Zhao et al., 2022; Liu et al., 2018) as following:

$$K_n = -k_c\delta\left[2\ln\left(\frac{R-\delta}{R}\right) - \frac{R}{R-\delta} + 1\right] \tag{10}$$

$$K_t = K_n/2(1+\nu) \tag{11}$$

ν), (11)

where k_c is barrier stiffness parameter from energetic barrier method (Zhao et al., 2022). ν is Poisson's ratio.

2.3. *Coupling between MPM and SDEM*

Fig. 4 illustrates the flow chart of the coupled MPM-SDEM algorithm. The interactions between MPM and SDEM can be separated into MP-face and MP-edge interactions, which are modeled as vertex-face and vertex-edge contact, respectively, as illustrated in Fig. 3. With these definitions, the MP-vertex interaction is treated as the MP-edge interaction. The simplification of treating MP-vertex contacts as MP-edge contacts is supported by the geometric and computational equivalence in sphero-polyhedra contact mechanics. Since a vertex can be regarded as the endpoint of a block edge, a unified edge-based contact algorithm can handle both edge and vertex interactions without separate computations (Galindo-Torres, 2013). This reduces algorithmic complexity and eliminates potential singularities in force calculations at point contacts.

To reliably define the contact between each possible pair, it is critical to determine the overlapping distance δ. Similar with Eq. (7), the overlapping distance $\delta_{\mathrm{MP-SDEM}}$ is expressed as following:

$$\delta_{\mathrm{MP-SDEM}} = R_p^0 + R_i - d(\mathrm{MP}, \mathrm{S}) \tag{12}$$

where $d(\mathrm{MP}, \mathrm{S})$ is the distance from the MP to the nearest point on the sphero-polyhedron surface, and R_p^0 is the initial radius of MP , calculated as follows:

$$R_p^0 = (3\Delta x^3/\mathrm{n_I}/(4\pi))^{1/3} \tag{13}$$

where Δx is the grid size, and $\mathrm{n_I}$ is the MP number per grid cell in the initial configuration. R_p^0 remains constant in the gasification state, where MP is treated as a disconnected, stress-free media with no tensile deformation and a dilation angle of 0 degrees (Dunatunga et al., 2015). In the dense state, strain of dry granular flows is less than 0.01, indicating that resulting radius change ($<$ 0.3%) can be negligible (Holtzman et al., 2009).

Once contact is identified, the coupling contact force $\boldsymbol{F}_{c,p}$ is calculated following the contact law from conventional DEM (see section 2.2). The obtained $\boldsymbol{F}_{c,p}$ is mapped to SDEM and MPM, respectively. In SDEM, the contact force $\boldsymbol{F}_{c,p}$ is applied to the nearest contact point. The coordinate and rotation angle of the SDEM particle is updated based on Newton's second law. In MPM, opposite $\boldsymbol{F}_{c,p}$ acting on the MPs is considered as external force exerted by SDEM particle and is mapped to the neighbouring grid nodes according to their respective weights to update $\boldsymbol{f}_c$ (Eq. (1), as follows:

$$\boldsymbol{F}_{c,I} = \sum_{p}^{n_p} w_I \boldsymbol{F}_{c,p} \tag{14}$$

$$V_I = \sum_{p}^{n_p} w_I V_p \tag{15}$$

$$\boldsymbol{f}_c = \boldsymbol{F}_{c,I}/V_I \tag{16}$$

where V_p is $m_0 J_p/\rho_0$, w_I is the weight of *I*-th node calculated by Eq. (2), $\boldsymbol{F}_{c,p}$ is coupling force $\boldsymbol{F}_c$ on *p*-th MP, V_p is volume of *p*-th MP, $\boldsymbol{F}_{c,I}$ is contact force mapped to grid node. V_i is the volume of *i*-th node. J_p is Jacobi of *p*-th MP, m_0: mass of MP, ρ_0 is density of MP.

$$\sum_{I=1}^{n_I} \boldsymbol{F}_{c,I} = \sum_{p=1}^{n_p} \boldsymbol{F}_{c,p}, \tag{17}$$

Regarding momentum conservation, the nodal weights $\mathrm{w_I}$ satisfy the

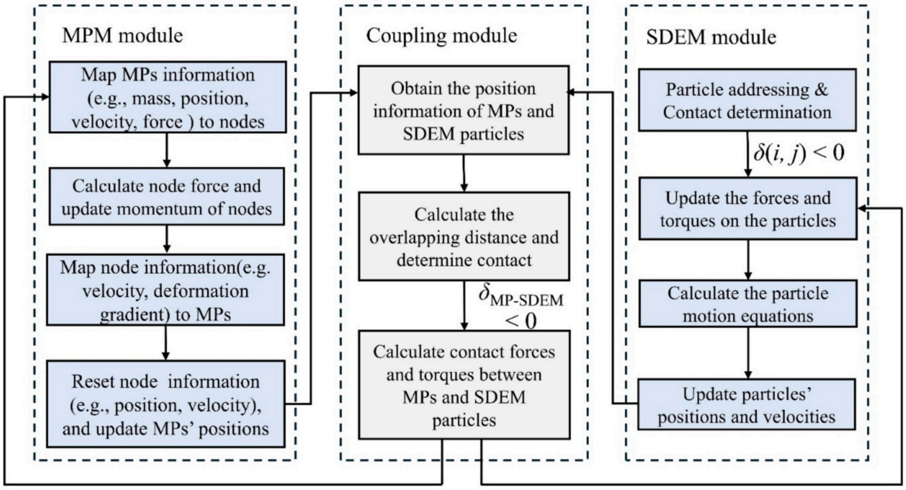

Fig. 4. Flow chart showing the MPM cycle, the SDEM cycle and the coupling between them at each timestep.

partition of unity property $\sum_{\text{I}} w_{\text{I}} = 1$ for each MP. This property is fundamental to the MPM shape functions and ensures that the total mapped contact force over all grid nodes is exactly equal to the sum of the original contact forces acting on the MPs:

$$\sum_{\text{I}=1}^{\text{n}} \boldsymbol{F}_{\text{c,I}} = \sum_{\text{I}=1}^{\text{n}} \sum_{\text{p}}^{\text{n}_\text{p}} w_{\text{I}} \boldsymbol{F}_{\text{c,p}} = \sum_{\text{p}}^{\text{n}_\text{p}} \boldsymbol{F}_{\text{c,p}} \sum_{\text{I}=1}^{\text{n}} w_{\text{I}} = \sum_{\text{p}}^{\text{n}_\text{p}} \boldsymbol{F}_{\text{c,p}} \tag{18}$$

In the MPM-SDEM context, the contact force $\text{F}_{\text{c,p}}$ is computed via DEM contact law at the MP-DEM particle interfaces. The force on the MP side is equal in magnitude and opposite in direction to that on the DEM side. Thus, the total impulse imparted to the MPM domain via the grid update ($\Delta t \sum_{\text{I}} \boldsymbol{F}_{\text{c,I}} = \Delta t \sum_{\text{p}} \boldsymbol{F}_{\text{c,p}}$) balances the opposing impulse on the DEM domain ($-\Delta t \sum_{\text{p}} \boldsymbol{F}_{\text{c,p}}$), ensuring global linear momentum conservation for the coupled system.

The force-mapping operation is a linear interpolation that neither artificially amplifies nor dissipates energy. Any energy dissipation observed in the coupled MPM–SDEM framework originates solely from the physical contact model, such as frictional sliding or damping dissipation. These mechanisms represent realistic interface behavior rather than an artifact of the mapping.

3. MPM-SDEM validations

The MPM solver employed in this study has been extensively validated in previous works (Dunatunga et al., 2015; Jiang et al., 2022). In the present work, we focus on validating the newly developed coupling framework between MPM and SDEM, as well as the accuracy of non-spherical object representation. The validation is performed through three independent benchmarks: a theoretical solution for a block sliding along a flume bed and experimental evidence of granular flows impacting single and multiple blocks. These tests specifically assess the robustness of the contact detection and force transmission at the MPM-SDEM interface. All simulations were run on a single NVIDIA RTX 3090 GPU (24 GB VRAM) using the Taichi programming language, which is optimized for high-performance numerical computations (Hu, 2018). Taichi can automatically parallelize outermost for-loops in kernels, enabling efficient execution on target architectures.

3.1. *Validation of SDEM: A theoretical solution for single block sliding along a flume bed*

The SDEM is used to simulate a rigid block sliding along a flume. The block is a cube with a side length of 0.1 m, generated in SDEM using a sphere of radius 0.005 m (see section 2.2). The flume bed, measuring 20 m in length, 1 m in width, and 1 m in thickness, is similarly constructed in SDEM with the same sphere radius of 0.005 m. Different basal friction coefficients ($\mu_b = 0$ and 0.1) and slope angles ($\theta = 10^\circ$, 20°, 30°, and 40°) are examined. The density is adopted as 3000 kg/m^3, and the barrier stiffness is set as 10000 N/m. The simulation duration is 2 s with a timestep of 5×10^{-6} s. The analytical solution for predicting travelling distance $S_\text{b}(t)$ of the block at any given time t can be calculated based on the Newtonian laws:

$$S_\text{b}(t) = \frac{t^2}{2}(gsin\theta - \mu gcos\theta) \tag{19}$$

Fig. 5a and Fig. 5b show the comparison between the calculated and computed travelling distances temporally of a block on a channel with $\mu_b = 0$ and $\mu_b = 0.1$, respectively. The close agreement demonstrates the ability of proposed SDEM for accurately simulating block sliding along the flume bed.

3.2. *Validation of MPM-SDEM: flow-type landslide impacting the single block*

3.2.1. *Flume experiment*

A physical experiment is carried out here using a flume (Fig. 6) with a length of 1.8 m and width of 0.2 m. The flume is widely used for modelling flow-type landslides (Fang et al., 2022 & 2023). A storage container at the upstream end of the flume is filled to form an initial column with length $L_i = 0.3$ m and height $H_i = 0.2$ m. The flume is inclined to 10°. A mass of 19 kg of glass spheres with a particle size of 0.002 m and a bulk density of 1600 kg/m^3 is used to simulate the flow-type landslide. The material in the storage container was released using a pneumatically controlled gate. A copper cube with a side length of 0.02 m was placed $L_0 = 0.21$ m downstream of the column. The friction coefficient between the flume and block is 0.67. A camera (model no.: GoPro HERO 11) that captures images at a frame rate of 60 frames per second was installed at the side of flume to record the flow kinematics and the position of the block through a transparent acrylic sidewall.

Fig. 7 shows the observed impact kinematics at four typical times. The flow direction is from the left to the right. It can be seen that after dam-break, the flow-type landslide accelerates under the influence of gravity and impacts the cube at $t = 0.3$ s. The flow-type landslide moves around the sides of the block and eventually exerts enough momentum to move the block. In addition to sliding, rotation is observed as well. The change in the travelling distance and velocity is shown in Fig. 8. Eventually the flow and block come to rest. These results can be used to

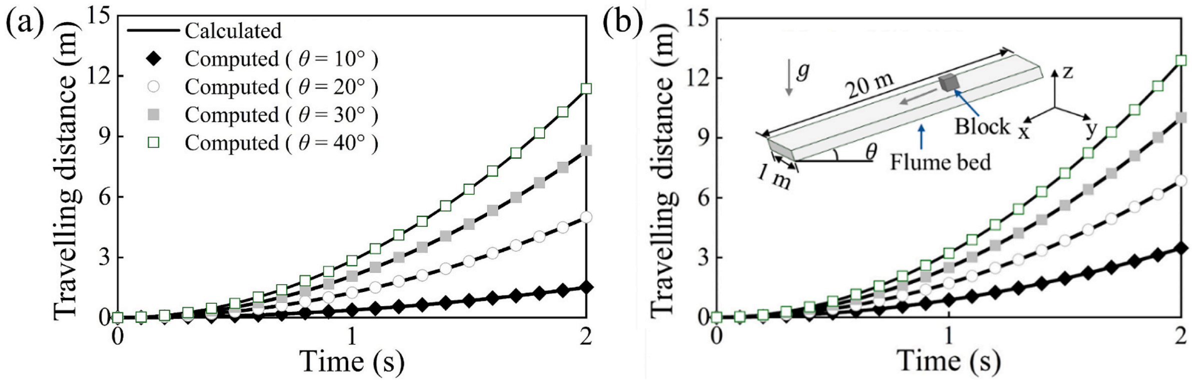

Fig. 5. Comparison of computed and calculated travelling distances for different basal friction coefficients: (a) $\mu_b = 0$; and (b) $\mu_b = 0.1$.

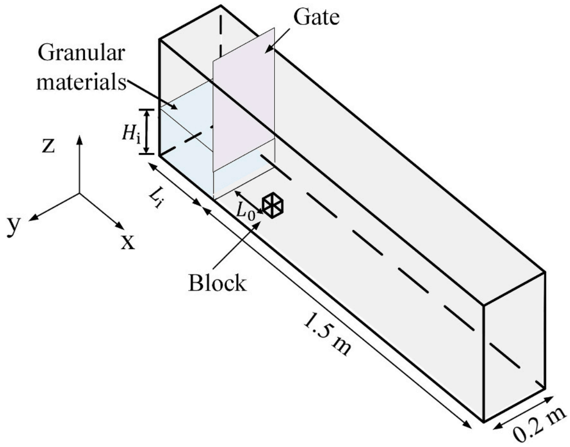

Fig. 6. Experiment setup for simulating a flow-type landslide impacting the single block.

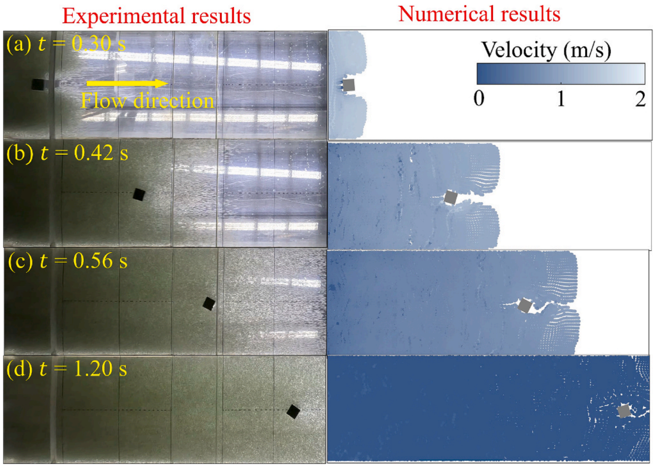

Fig. 7. Comparison of flow kinematics between measured and computed results.

benchmark the reliability of the coupled MPM-SDEM.

3.2.2. *Comparison between calculated and measured results*

The simulation setup modelled by MPM-SDEM are identical to those in the flume tests. For particle–particle interactions in MPM, the Young's modulus and Poisson's ratio in the calculation are $E = 1$ M Pa and $\nu = 0.3$, respectively (Ng et al., 2020). In addition, the internal friction coefficient is set as 0.24, basal friction coefficeint is used as 0.21, the dynamic friction coefficient is set as 0.65, and the bulk density is 1600 kg/m^3, according to the properties of the glass spheres. The copper cube modelled using SDEM has the same properties as that used in the flume experiments with friction coefficient of 0.67 and density of 8900 kg/m^3. Parameters related to the mechanical and contact behavior of the flow-block interaction are summarised in Table 1. To obtain high-fidelity input parameters of basal friction coefficient and maximum dynamic friction, the genetic algorithm (GA) is used. The procedure of the adopted GA is detailed in Appendix C. And a sensitivity analysis about the sphere radius in SDEM particle has been discussed in Appendix D.

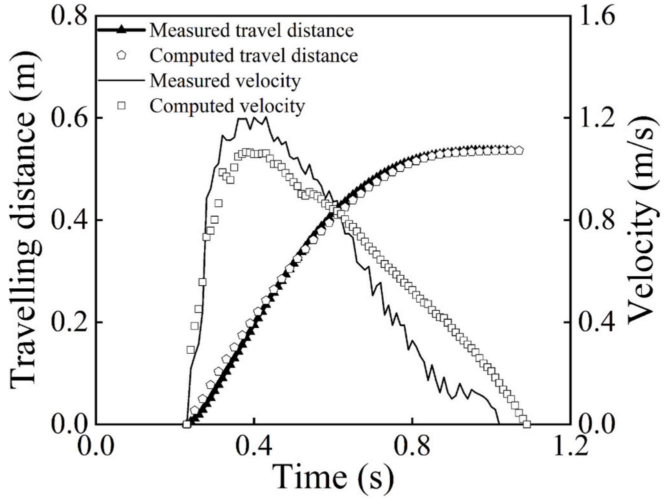

Fig. 8. Comparison of travelling distance and travelling velocity between measured and computed results.

Consistent with the flume experiments, the glass spheres are

Table 1
Summary of input material parameters: flow-type landslide impacting block.

Parameter	Value	Source
Particle density	1600 kg/m^3	Measured
Internal friction coefficient of particles	0.24	Measured
Basal friction coefficient of particles	0.21	Calibrated
Gravitational acceleration	9.81 m/s^2	Ng et al., 2020
Maximum dynamic friction coefficient	0.65	Calibrated
Young's modulus	1 MPa	Ng et al., 2020
Poisson ratio	0.3	Ng et al., 2020
Blending ratio	0.99	Stomakhin et al., 2013
Block density	8900 kg/m^3	Measured
Basal friction coefficient of block	0.67	Measured
Barrier stiffness	10000 N/m	Jiang et al., 2022

generated in the storage container by MPM. The background grid is composed of cubic cells with a side length of 0.01 m, each containing 8 material points, resulting in a total of 96,000 material points. The block and flume bed are modelled as SDEM. A gravitational acceleration of 9.81 m/s^2 is applied to the entire computational domain and elements.

Fig. 7 shows a comparison between the measured and computed flow kinematics. The MPM-SDEM model captures the entire process of the flow impacting the block, reproducing the rotation of the cube as well. In addition, the measured and computed travelling distance and velocity with time are shown in Fig. 8. It is evident from Fig. 8 that the computed travelling distance of the block by MPM-SDEM shows close agreement with experimental results, with the difference of terminal travelling distance less than 0.8%. The close agreement between the numerical and experimental results underscores the capability of the newly-proposed MPM-SDEM method to accurately capture the flow-block interactions, providing the valuable predictions into flow-type landslide hazards. It is worth noting that uncertainties in measured travelling distance, arising from Camera distortion and manually controlled dam-break initiation, may affect the agreement between computed and measured travelling distance.

3.2.3. *Impact force exerted on block*

The total impact force F_t originates from the flow-type landslide impacting the edge of a block F_e and its face F_f, as shown in Fig. 9. Overall, the total impact force F_t first exhibits a rapid increase to a peak, then reduces to 0.32 N around 0.4 s. After that, it fluctuates around 0.20 N with multiple spikes before being stable. The evolution of impact force F_f is closely consistent with that of the total impact force F_t. Compared with F_f, the impact force on the edge F_e exhibits smaller variations in amplitude over time due to less efficiency in bearing impact from flowing material. The decomposition of impact force provides potential to enhance understanding of localized impact force distributions during flow-structure interactions. By separately analyzing forces on different parts of the block, it allows more precise identification of vulnerable zones, which can inform reinforcement strategies in protective structures for landslide-prone areas.

The ratio F_f/F_t is shown in Fig. 9, which quantifies the contributions of the block face to the total force. At the initial impact ($t = 0.25$ s), F_f/F_t reaches its maximum value of 0.8, corresponding to the face being perpendicular to the flow direction (see Inset d1). As block rotates, the decreases is observed in F_f/F_t. When the block rotation reaches 45° at $t = 0.72$ s, the minimum F_f/F_t is recorded (see Inset d2). With continued rotation, the edge of block deviates from the frontal normal impact, enabling face of block to undergo more flowing impact. This geometric switching drives a marked increase in in F_f/F_t (see Inset d3). Specifically, when the block's face is perpendicular to flow direction (Inset d1), it bears approximately 82% of the total impact force. In contrast, when block is rotated to 45° (see Inset d2), the face contribution decreases to 65%. It is evident that impact force distribution is strongly controlled by block's orientation. In addition, block shape should be a main consideration in determining F_f/F_t, which warrants further studies.

To evaluate the impact force exerted on the structures, the hydrodynamic model was proposed (Hungr et al., 1984; Jóhannesson et al., 2009; Song et al., 2022). It is assumed that the impact force is related to the impact area A, flow density ρ_f, flow velocity v_f, and flow depth h, as following:

$$F_t = \alpha_f \rho_f {v_f}^2 A \tag{20}$$

where α_f is the dynamic pressure coefficient, which is empirically found to be the function of Froude number Fr: $\alpha_f = 10.8\ Fr^{-1.3}$ (Thibert et al., 2008). Fr quantitatively characterizes the flow regimes: $Fr = v_f/\sqrt{gh_f}$. The computed impact force on the block is validated based on the hydrodynamic model, as shown in Fig. 9. The calculated total impact force exhibits consistency with that computed: rapidly rise to the peak in the initial phase, followed by a sharp decline with oscillations gradually stabilizing, reflecting the dynamic process of flow-type landslide impacting a block. The theoretical value consistently exceeds the computed F_t, serving as a conservative upper bound. The computed impact force agrees reasonably well with the calculated, with peak positions coinciding and decay curves morphologically akin. This demonstrates the reliability of the proposed MPM-SDEM model in this study for the flow-type landslide impacting the single block.

3.3. *Validation of MPM-SDEM: flow-type landslide impacting the multiple blocks*

3.3.1. *Numerical model validation*

The MPM-SDEM is further validated by the results of flume test by Liu et al. (2018), which investigated a granular flow impacting the three stacked wooden blocks. All the geometries simulated in MPM-SDEM are consistent with those in the flume test, as detailed by Liu et al. (2018). The experimental flume consists of a Plexiglas tank, measuring 600 mm long, 200 mm wide, and 300 mm high. The incoming granular is confined at the top of the flume to form a region of 100 × 200 × 200 mm^3. Three identical wooden blocks with 20 × 198 × 18 mm are stacked and positioned 200 mm downstream of the deposited granular material. The bottom block is glued to the channel bed to prevent motion. Parameters related to the mechanical and contact behavior of the flow-block interactions are summarised in Table 2.

Fig. 10 shows the comparison of flow kinematics observed from

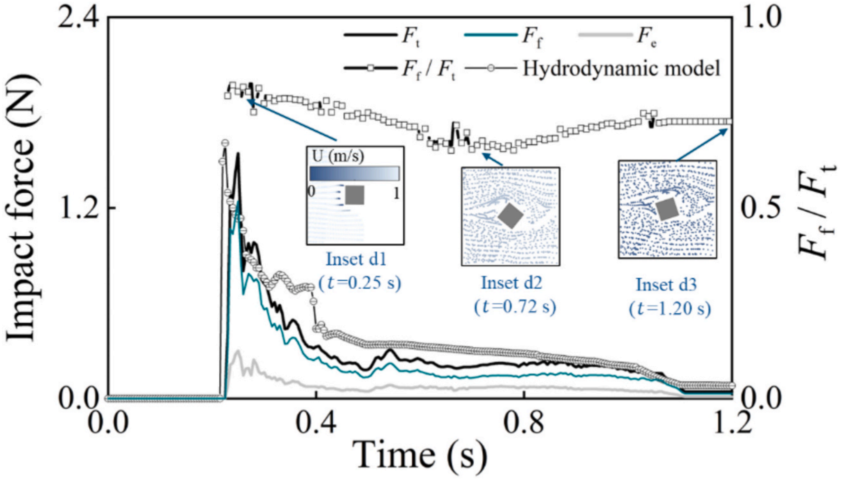

Fig. 9. The impact force–time history.

Table 2
Summary of input parameters for flow-type landslide impacting multiple blocks.

Parameter	Value	Source
Flow density	1300 kg/m^3	Liu et al., 2018
Internal friction angle	22 °	Liu et al., 2018
Basal friction coefficient	0.13	Calibrated
Gravitational acceleration	9.81 m/s^2	Ng et al., 2020
Maximum dynamic friction	0.60	Calibrated
Young's modulus	50 kPa	Liu et al., 2018
Poisson ratio	0.40	Liu et al., 2018
Blending ratio	0.99	Blatny et al., (2025)
Density of block	500 kg/m^3	Liu et al., 2018
Basal friction coefficient of block	0.60	Liu et al., 2018
Barrier stiffness	10000 N/m	Jiang et al., 2022

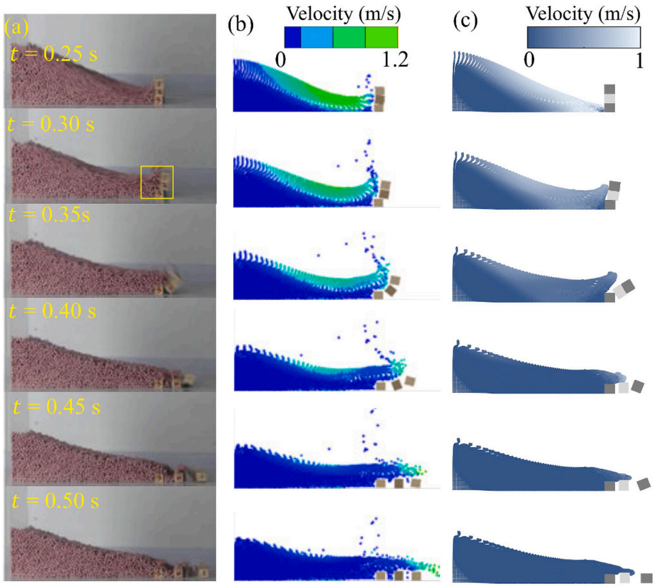

Fig. 10. Flow kinematics of flow-type landslide impacting the multiple blocks: (a) Experimental study (Liu et al., 2018); (b): MPM simulation (Liu et al., 2018); (c) MPM-SDEM simulation.

experimental measurements, and numerical simulations by the MPM-SDEM solver in this study. The incoming granular material impacts the block at $t = 0.\ 25$ s, causing the upper two blocks to rotate around the bottom one. At $t = 0.\ 40$ s, the middle block falls onto the flume bed, followed by the top block impacting the block at about 0.5 s. Evidently, the entire process is well captured by MPM-SDEM model. When the flow ceases, the differences between the measured and computed (MPM-SDEM) travelling distances are 1.4% for the middle block and 3.9% for the top block, respectively. For comparison, the results from MPM is also shown in Fig. 10. Compared with MPM-SDEM, MPM provides poorer agreement with experimental observations, especially in reproducing the motion of the blocks, with the differences in travelling distance for the middle and top blocks of 2.3% and 5.0%, respectively. This can be attributed to dependence of MPM on fixed background grids for the momentum exchange between flowing material and block, which fails to capture the block rotation. These results highlight the robustness and reliability of the MPM-SDEM framework in simulating complex granular-blocks interactions.

3.3.2. *The calculated impact force on the blocks*

Fig. 11 shows the computed impact force on the three blocks. After the impact of incoming granular material against the block, the impact force is firstly detected on the bottom block, rapidly rising to a peak value of 9.72N. Subsequently, the impact force attenuates to the static force due to the self-weight of the granular material depositing in front of the block. Different from the bottom block, the peak impact forces on the middle and top blocks are significantly reduced, with the difference up to 50% and 80%, respectively. Previous study (Yu et al., 2024) has similarly noted that peak impact pressure is always recorded by the sensor at the base of the dam. Another difference is that, after the peak impact, the impact force reduces to zero. Evidently, the MPM-SDEM effectively characterizes the impact force on the block, offering valuable insights for mitigating flow-type landslide hazards. For validation, the theoretical impact force (Eq. (20) acting on the bottom block is also calculated (black line in Fig. 11). As can be seen, the computed results by the proposed MPM-SDEM herein show reasonable agreement with the calculated results, with a peak impact force of 10.6 N.

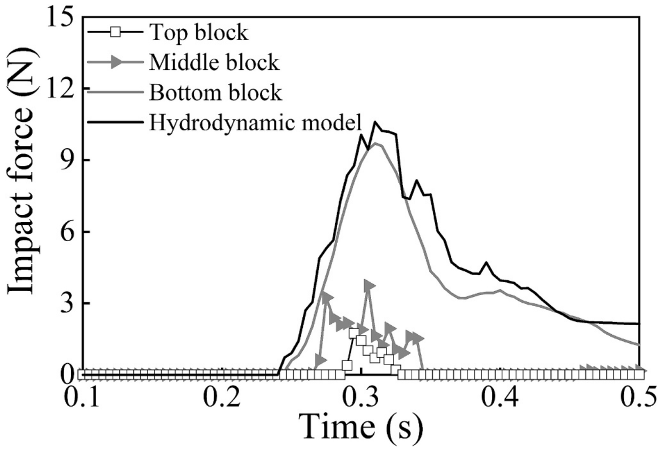

Fig. 11. Computed impact force–time history of three blocks.

4. Comparison between MPM-SDEM and MPM-LSDEM

In this section, the proposed MPM-SDEM method is compared with the conventional MPM-LSDEM method, based on the test of a granular flow impacting multiple blocks. In addition, the computational efficiency is compared by simulating head-on collision between two blocks and flow-type landslide-block interactions, including scenarios with a single block and multiple blocks.

4.1. *MPM-SDEM vs. MPM-LSDEM*

The physical experiment, as detailed in the section entitled 'Validation of MPM-SDEM: flow-type landslide impacting the multiple blocks', is also used here as a benchmark to quantify the computational accuracy of MPM-SDEM and MPM-LSDEM. In contrast to SDEM, the surface of a particle in LSDEM is discretized into a set of nodes, also called as node-to-surface approach (Choi, 2024).

Fig. 12 compares the flow kinematics of physical experiment (Fig. 12a), MPM-SDEM (Fig. 12b) and MPM-LSDEM (Fig. 12c). The clear differences can be observed. For example, at $t = 0.40$ s, it is observed from Fig. 12a2 that the middle block falls onto the flume bed. In comparison with MPM-LSDEM (Fig. 12c2), the result of MPM-SDME (Fig. 12b2) provides a better approximation. In addition, at $t = 0.45$ s and $t = 0.50$ s, the top block is adjacent to the middle block in MPM-LSDEM (Fig. 12c3 and Fig. 12c4), which indicates a clear discrepancy from physical experiment (Fig. 12a3 and Fig. 12a4) and MPM-SDEM (Fig. 12b3 and Fig. 12b4). To further evaluate the computational accuracy of both numerical methods, the travelling distance of the upper two blocks is analyzed. The difference between measured and computed travelling distances for the top block is 10.7% for MPM-LSDEM and 4.0% for MPM-SDEM, respectively, while for the middle block, the differences are 1.7% for MPM-LSDEM and 1.4% for MPM-SDEM, respectively. Evidently, improvement in predicting travelling distance by

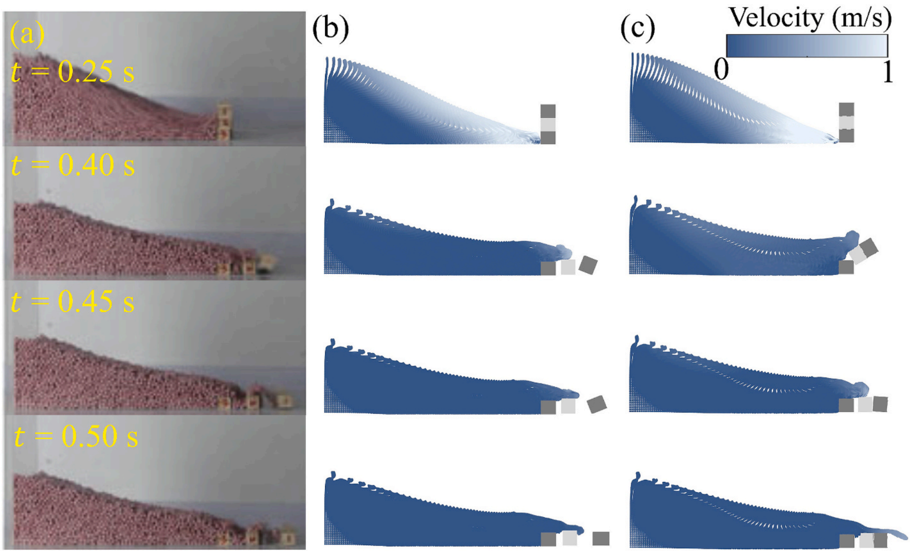

Fig. 12. Flow kinematics of flow-type landslide impacting the multiple blocks: (a) Experimental study (Liu et al., 2018); (b) MPM-SDEM simulation; (c) MPM-LSDEM simulation.

MPM-SDEM is up to 63% and 18% for top and middle blocks, respectively. These findings underscore the robustness and reliability of the MPM-SDEM framework in simulating flow-type landslide-blocks interactions.

The abovementioned discrepancies may be attributed to the distinct contact detection algorithms used in two numerical methods. In the MPM-LSDEM framework, contact is detected by identifying whether multiple surface nodes of a particle intrude into another particle (Zhao et al., 2023). This node-based method is prone to cause chattering, force oscillations, and incorrect force directions in multi-contact configurations, particularly when nodes slide along edges or vertices (Feldfogel et al., 2024). In contrast, in the MPM-SDEM framework, the block is simulated as an SDEM particle with spherical surface, allowing the adoption of a robust, exact sphere-to-sphere contact algorithms. As a result, the resulting contact forces are smoother, better oriented, and exhibit significantly reduced numerical noise (Galindo-Torres, 2013). The improved contact solution for particle–particle interactions enables MPM-SDEM to effectively replicate flow-type landslide dynamics.

4.2. *Computational efficiency*

Head-on collisions between two blocks with dimensions of 0.1 m and 0.3 m are simulated, respectively. All other parameters related to mechanical and contact behavior are kept identical. The initial distance between their centroids is 0.4 m. A prescribed initial velocity of 1 m/s is assigned to both blocks. The size ratio of sphere radius/node to the side length of block is set to 1/20. The computational costs for LSDEM and SDEM are 104 s and 87 s, respectively, indicating a 16.4% improvement in computational efficiency for SDEM compared to LSDEM. This can be attributed to the different contact approaches for generic irregular shaped particles. In LSDEM, the particle surfaces are discretized into 602 nodes, requiring 174 iterations per timestep for contact detection. However, in SDEM, each particle comprises 8 vertices, 12 edges, and 6 faces, with three contact types: vertex-face, edge-edge, and vertex-edge (see Fig. 3). For parallel block collisions, only vertex-face contact occurs, necessitating just four iterations at one timestep for contact calculations in SDEM. This efficient contact detection enhances computational efficiency of SDEM, which can be amplified as the number of non-spherical particles increases.

This study further evaluates the computational efficiency through flume tests of flow-type landslide impacting blocks with varying numbers of blocks. Fig. 13 illustrates the comparison of computational cost between MPM-LSDEM and MPM-SDEM methods. With the increasing number of the blocks, the computational efficiency is improved from 17% to 97%. With the increasing number of the blocks, MPM-SDEM achieves efficiency gains from 17% to 97%, consistently outperforming MPM-LSDEM across all tests. Evidently, the advantage of MPM-SDEM becomes more significant with increasing non-spherical particles in terms of computational efficiency, owing to its more efficient contact detection.

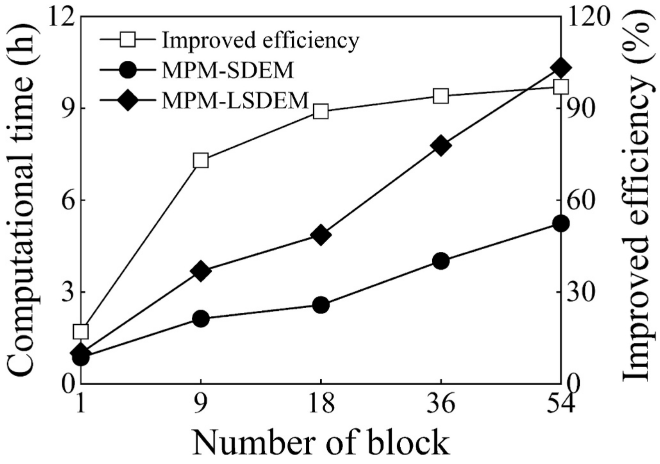

Fig. 13. Comparison of computational cost between MPM-LSDEM and MPM-SDEM.

5. Insights on the flow-type landslide impacting block

In this section, the calibrated MPM-SDEM solver is used to investigate the effects of the initial column height and initial distances between the column and the block.

5.1. *Simulation procedure*

The geometries of numerical model and the parameters related to the particle adopted in the MPM-SDEM modelling are identical to those reported in the section titled ‘Validation of MPM-SDEM: flow-type landslide impacting the single block’, except that a cube with height h_b

of 0.05 m is used here. The initial granular column is characterized by the initial aspect ratio AR $= H_i/L_i$, where H_i is its initial height and L_i is its initial length along the flow direction. AR varies from 1.3 to 4.0 to span low to tall columns, and the initial block-to-column distance L_0 from 4 h_b to 74 h_b to obtain a wide range of Froude numbers. In total, 20 simulations were carried out. Before the impact tests, the free-flow tests without the block were conducted to calibrate the flow velocities v_f and flow depths h_f (Choi et al., 2017), which serve to evaluate the flow properties reaching the block. The Froude number was then calculated, ranging from 1.04 to 11.82, which falls within the range of geophysical flows in field (Hübl et al., 2009). Based on the observed flow kinematics, it was found that when $h_f < h_b$, the block is partially submerged, while the block is completely buried by incoming flow when $h_f > h_b$. The calibrated flow thickness is plotted in Fig. 14, within the full controlling parameters investigated.

5.2. Observed kinematics

Fig. 15 shows a comparison of the computed kinematics of flow-type landslides impacting a rigid block under different initial aspect ratios (AR = 1.3 and 3.0) and normalized block-to-column distances ($L_0/h_b =$ 4 and 54). For each case, top and side views are shown, with flow moving from left to right.

For case with AR = 1.3, L_0/h_b= 4 (Fig. 15a), the column collapses under gravity and rapidly spreads along the bed. At $t = 0.22$ s, the flow impacts the block, forming a localized high-pressure zone upstream the block due to intensified collision between flowing material and block. The flow is deflected symmetrically around the block, forming a bow shock upstream and a granular vacuum downstream, resulting from that the block interrupts the upstream material supply and lateral spreading become dominant. At $t = 0.50$ s, flowing material overtops the block and fills the vacuum, shrinking it progressively. Overtopping occurs once the pile-up height exceeds the block crest, converting kinetic energy to potential energy. The block becomes fully submerged, with a flow thickness-to-block height ratio of about 2.31. At $t = 0.50$ s, both translation and rotation are evident, driven by asymmetric momentum transfer: upstream impact force drives forward motion, while uneven lateral frictional shear induces rotation. In contrast, for case with AR = 3.0, $L_0/h_b = 4$ (Fig. 15b), the larger initial column height increases potential energy, producing higher velocities and a thicker flow. Similarly, the block fully immerses into flowing material. The thicker overlying layer enhances overtopping and overburden pressure, increasing basal frictional resistance, which in turn inhibits block rotation. In Fig. 15c (AR = 1.3, $L_0/h_b = 54$), the extended channel allows pre-impact spreading and thinning, forming a high-speed, shallow leading edge. The recorded maximum pileup height remains below the block height, preventing full overtopping and leading to only partial submersion. This is also supported by the value of$h_f/h_b = 0.31$ (< 1.0). Evidently, a large L_0/h_b reduces the risks of block burial. Furthermore, compared to Fig. 15b, the block experiences greater disturbance due to the more impact energy transferred into block with increasing L_0/h_b.

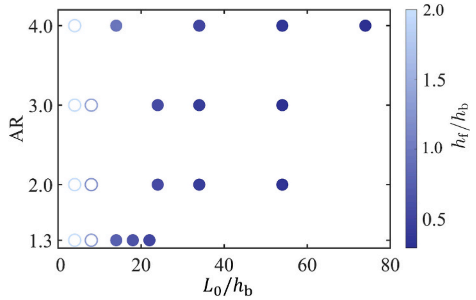

Fig. 14. Initial aspect ratio AR and normalized block-to-column distance L_0/h_b used in simulations. Colors indicate the calibrated flow thickness, normalized by block height h_b. Open circles indicate the block is absolutely submerged by flow-type landslide. Closed circles indicate the block is partially submerged by flow-type landslide.

5.3. Impact force on block

The impact force drives the mobility of the block. Fig. 16a shows the evolution of normalized impact force F_{peak}/F_{static} as a function of the normalized block-to-column distance L_0/h_b for different initial aspect ratios AR. Here F_{peak} and F_{static} are the maximum impact force and static impact force, respectively. Static force is mainly from the self-weight of the intercepting mass resting on the block. Regardless of AR, the ratio F_{peak}/F_{static} generally exhibits a slight increase at low L_0/h_b, before approaching an approximately constant level as L_0/h_b increases. A key distinction emerges based on block submerge states: in completely submerged cases ($h_f > h_b$), where the flow depth exceeds block height, the ratio F_{peak}/F_{static} is consistently smaller compared with partially submerged scenarios ($h_f < h_b$). This can be attributed to the fact that compared with completely submerged cases, the dynamic impact force of partially submerged scenarios tends to be enhanced but the static pressure is reduced due to extended channel accelerating mobility and promoting thinning flow. Note that the ratios F_{peak}/F_{static} of partially submerged cases only show a slight fluctuation. In other word, in this study, increasing L_0/h_b has a limited influence on the F_{peak}/F_{static} of submerged cases Furthermore, F_{peak}/F_{static} shows a positive correlation with AR, where increasing AR leads to larger F_{peak}/F_{static}. This stems from greater material supply and potential energy in taller columns, posing greater risks to bury block.

Fig. 16b shows the effects of Froude number on the normalized impact force F_{peak}/F_{static}. A theoretical model has been developed by Ng et al. (2021) to predict F_{peak}/F_{static} for closed intercept dam, which is shown in Fig. 16b, as following:

$$\frac{F_{peak}}{F_{static}} = 1 + \frac{2\alpha_f}{k} Fr^2 \tag{21}$$

In this model, it is assumed that peak impact force is calculated by the hydrodynamic model (Eq. (20), and static impact force is given by the hydrostatic model: $0.5k\rho_f h_f A$, where k is the empirical static pressure coefficient. Both dynamic pressure coefficient α_f and static pressure coefficient k are typically used to account for the uncertainties in the flow composition, natural environment, barrier type, and impact dynamics (Song et al., 2017; Poudyal et al., 2019). Their values can be case-specific and depends on the experimental setup and controlling parameters. A theoretical bounding reference line from Eq. (21) is provided with $k = 1$ (no internal shear strength) and $\alpha_f = 1$ (inelastic collision). Similarly, the ratios F_{peak}/F_{static} for dry granular flows impacting the closed dam in the previous literature (Caccamo et al. 2012) are also compared here. In this study, the F_{peak}/F_{static} exhibits positive correlation on Froude number, which follows the trend from the experimental results of flows impacting the closed barrier. In contrast, normalized impact forces exerted on block in this study are smaller than these against the closed dam. The block can be assumed as the dam with limited width, which is less efficient to bear the impact force compared to the closed dam. To further quantify the linkage between F_{peak}/F_{static} and Fr, Eq. (21) is adopted to fit our force data with $k = 1.6$ and $\alpha_f =$ 0.18.

It can be seen that the impact force model can capture the dependence of F_{peak}/F_{static} on Froude number, but struggle to accurately predict the value of F_{peak}/F_{static}. Although so, the impact force model (Eq. (21) can still serve as a reference to predict impact loads on the block.

5.4. Energy transfer and dissipation

This section provides a new insight to understand the interactions

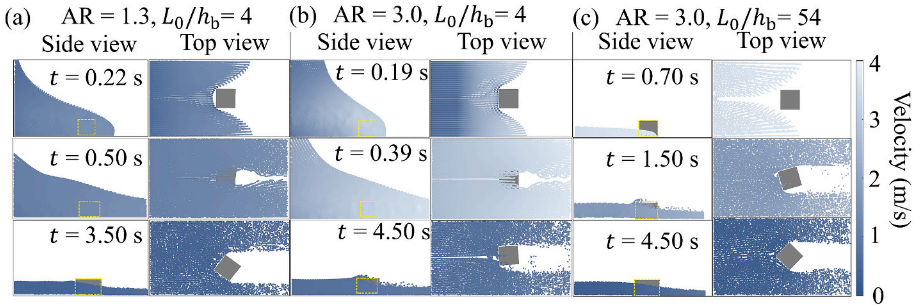

Fig. 15. Typical snapshots of flow kinematics for three typical cases (a) AR = 1.3; $L_0/h_b = 4$; (b) AR = 3.0; $L_0/h_b = 4$; and (c) AR = 1.3; $L_0/h_b = 54$. Yellow dash line indicates the side contour of the block.

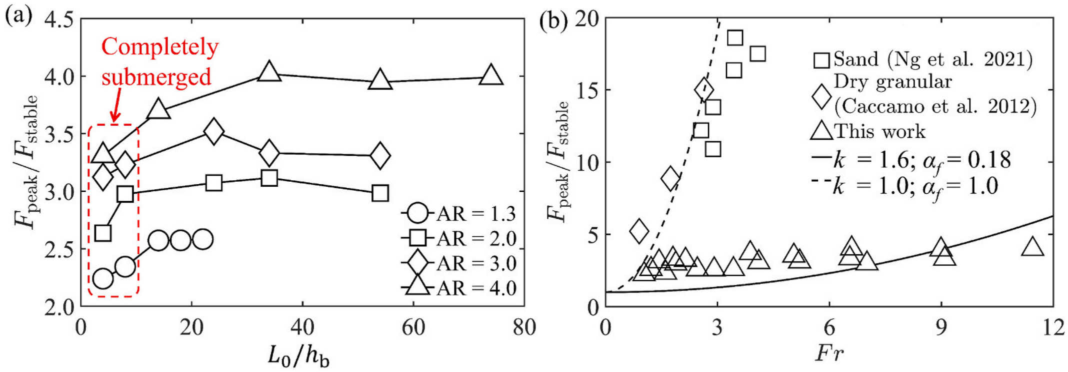

Fig. 16. (a) Comparison of normalized impact force F_{peak}/F_{static} for different initial aspect ratios and initial block-to-column distances; (b) Comparison of the influence of Froude number on normalized impact force.F_{peak}/F_{static}

between flow-type landslide and the block by examining the energy transfer and dissipation. Fig. 17 shows the temporal evolution of normalized energy by the initial potential energy for both flow-type landslide and block. As shown, upon initiation, the potential energy of flowing material is gradually converted into kinetic energy. The kinetic energy of flowing material exhibits a characteristic rapid rise to a peak, followed by a slight decline and subsequent moderate recovery, as evidenced by synchronized peaks at approximately $t = 0.38$ s two different cases in Fig. 17. The post-peak decrease in kinetic energy can be attributed to collapse kinematics, including vertical free-fall and lateral spreading (see insets in Fig. 17b), where descending particles collide with lower lateral spread part, dissipating energy via inelastic interparticle interactions and frictional shear. Dissipated energy monotonically accumulates, reaching 77% in the completely submerged case (Fig. 17a) and 73% in the partially submerged case (Fig. 17b) at $t = 4.5$ s, when the system approaches quasi-steady state. The disparity arises from different interactions between flow-type landslide and the block.

Due to the momentum exchange, the block can be driven by the flowing material. The kinetic energy of block rapidly increases and decreases, consistently remaining a small portion of initial potential energy (<0.4%). Fig. 18 shows the $E^b_{k,max}/E^f_{p,0}$ for different L_0/h_b, revealing a bilinear trend: an initial decrease followed by an increase for fixed AR. Because Larger L_0/h_b facilitates enhanced momentum transfer via higher pre-impact velocities from extended acceleration, yielding greater block speeds. However, L_0/h_b also controls immersion state (see Fig. 14). Complete submersion thickens the overtopping layer, enhancing overburden stresses and frictional drag, which counteracts translation and rotation. This competitive interplay, which is between amplified impact momentum and increased resistance, regulates the bilinear evolution, with minimum value of $E^b_{k,max}/E^f_{p,0}$ occurring at transitional L_0/h_b where resistance dominates. Throughout, AR exerts a

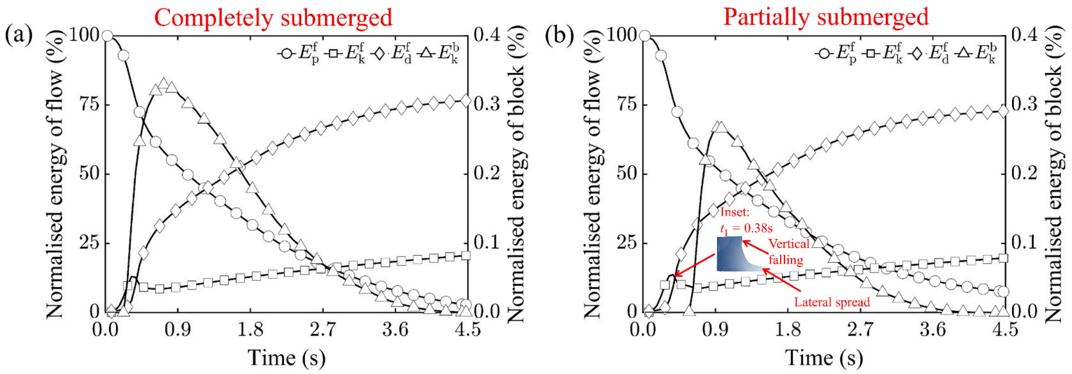

Fig. 17. Evolution of normalized energy for two different cases: (a) AR = 3.0, L_0/h_b=4; (b) AR = 3.0, L_0/h_b = 24. E^f_p, E^f_k and E^f_d are the potential energy, kinetic energy and dissipated energy of flow-type landslide, respectively. E^b_k is the kinetic energy of the block.

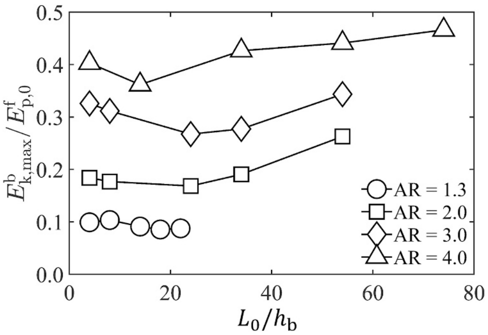

Fig. 18. Comparison of normalized maximum kinetic energy for the block across different initial aspect ratios and initial block-to-column distances.

consistently positive influence, as higher AR enhances initial potential energy and inertial forces, sustaining greater kinetic energy via thicker, faster flows that overwhelm frictional losses.

5.5. *Travelling distance of the block*

Predicting travelling distance of the block is a main concern in assessing flow-type landslide-induced hazards. In this section, the attempt to relate the travelling distance of the block to flow kinematics as quantified by Froude number, has been conducted. As shown in Fig. 19a, travelling distance S_b, normalized by initial block-to-column distance L_0, exhibits relatively weak correlation with the Froude number. S_b/L_0 can be separated into two regions based on block submersion states. Linear regressions are fitted to the computed data. For completely submerged cases (circles), a weak positive dependence is observed with a Pearson correlation coefficient r = 0.02. In contrast, partially submerged cases (squares) show a weak negative dependence with r = -0.11. The overall dispersion highlights the insufficiency of the standard Froude number in capturing block travelling distance, likely due to the interplay of multiple flow characteristics, such as velocity and depth, which complicate flow-block interactions.

In order to better identify the governing parameters related to block travelling distance, it is regarded as the function of seven key variables, as following:

$$S_b = f_1(v_f, h_f, L_0, h_b, g, \rho_f, \rho_b) \tag{22}$$

where f_1 is an unknown function, ρ_b is block density. By dimensional analysis, guided by Buckingham's π theorem, the general functional relationship can be reformulated in the dimensionless form:

$$\frac{S_b}{L_0} = f_2\left(\frac{v_f}{\sqrt{gL_0}}, \frac{h_f}{L_0}, \frac{h_b}{L_0}, \frac{\rho_f}{\rho_b}\right) \tag{23}$$

where f_2 is a new unknown function, and $v_f/\sqrt{gL_0}$ represents a modified Froude number Fr_1, using the free flow length (i.e., block-to-column distance) L_0 as the macroscopic characteristic length scale instead of flow depth h_f. L_0 represents the macroscopic length over which the flow accelerates under gravity prior to impact, encapsulating the cumulative effects of initial potential energy conversion, flow spreading, and velocity buildup. In contrast, flow thickness h_f is a local, instantaneous measure of flow thickness at the point of impact, which is highly sensitive to transient phenomena, such as flow thinning during propagation. A larger L_0 allows the flow to obtain a higher velocity and a smaller flow thickness before impacting on the block. By incorporating L_0, Fr_1 implicitly accounts for these upstream dynamics. The modified Froude number may have the potential to provide a more robust framework for displacement predictions. Physically, Fr_1 can be interpreted as the ratio of flow velocity v_f to the gravitational wave speed along the downstream direction $\sqrt{gL_0}$, or alternatively, the ratio of the time $\sqrt{L_0/g}$ for material to move downwards under gravity to impact the block and the time $\sqrt{L_0/v_f}$ for a flow to travel flume length L_0 at velocity v_f. Fig. 19b shows the influence of modified Froude number on the normalized travelling distance, revealing the strong linear correlations for completely (r = 0.91) and partially (r = 0.83) submerged cases. Evidently, Fr_1-driven scaling law governs the impacts of flow-type landslide on the block in both submersion regimes. This enhanced predictability suggests that the modified Froude number may incorporate corrective factors, such as flow thinning and velocity variability, providing a more robust framework for displacement predictions.

6. Implications for flow-type landslide hazard mitigation

In this study, the SDEM particle is used to simulate non-spherical blocks, demonstrating its potential for broader application to particles with complex geometries. In particular, real-world flow-type landslides and objects typically exhibit complicated behaviors. Recent researches highlight that particle shape significantly influences the physical behaviors, including segregation (Cúñez et al., 2024), particle breakage (Konrad et al., 2018; Liu et al., 2025), and rheology (Mandal et al., 2018), but a general method to accurately capture the particle shape is still missing. The proposed SDEM method provides a robust alternative. In particular, compared with clump-based methods (Angelidakis et al., 2021) and node-to-surface approaches (Lai et al., 2023), the SDEM method provides a better computational efficiency due to efficient contact detection algorithm.

It has been demonstrated that the proposed MPM-SDEM model can reliably predict the travelling distance and impact force of flow-type landslide. This capacity broadens its applicability to simulating flow-type landslide interactions with the protective structures, such as closed barrier, slit dam and baffle arrays (Fang et al., 2023), where precise estimation of kinematic behavior and loading is critical for effective interception design. Such simulations often require long-

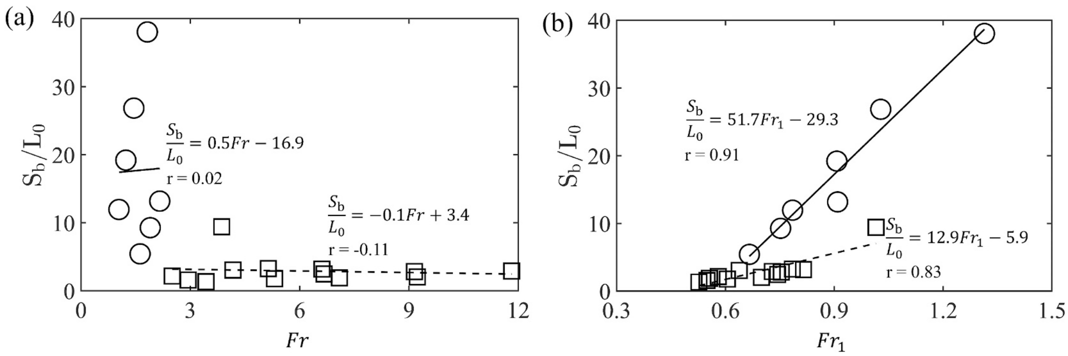

Fig. 19. (a) Normalized travelling distance S_b/L_0 versus Froude number Fr; (b) Normalized travelling distance S_b/L_0 versus modified Froude number Fr_1. Circles indicate that the block is completely submerged. Squares indicate that the block is partially submerged.

duration and large-scale computations, posing significant challenges to develop numerical methods. By coupling MPM for continuum flow and SDEM for rigid structures, the proposed method efficiently addresses these challenges. This positions MPM-SDEM as a valuable tool for optimizing the design of flow-type landslide mitigation structures.

Despite its strengths, the current MPM-SDEM model only focuses on single-phase flow-type landslides, limiting its applicability to two-phase landslides. Unlike single-phase flows, where mechanical inter-particle interactions dominate, two-phase flows exhibit distinct behaviors due to the presence of liquid within their pores. Solid-fluid interaction can regulate the Coulomb friction within and at the boundary of a flow-type landslide and thus influence its dynamics (Iverson and George, 2014). In addition, in this work, we only focus our attention on a single, rigid block, limiting its applicability to more realistic scenarios involving multiple, potentially deformable objects of varying shapes and sizes. It has been observed that interactions among diverse blocks can lead to complex fragmentation and redistribution of forces during flow-type landslides, thereby altering overall flow behavior and impact dynamics (Fang et al., 2021). Extending the model to incorporate two-phase flow-type landslides and multiple breakable blocks with heterogeneous properties will broad its application in simulating real-world geohazards, thereby providing insights in mitigation strategies.

7. Conclusions

This study presented details of a coupled MPM-SDEM solver for simulating the transport and burial of non-spherical objects by flow-type landslides. By combining SDEM for detailed object modeling with MPM for flow-type landslide, and incorporating an efficient sphere-smoothing contact algorithm, the method enables accurate computation of interactions while maintaining computational efficiency. Validations against theoretical sliding solutions and experimental benchmarks confirm its robustness to accurately predict the travelling distance of the block and impact force on them. Furthermore, a comparison between MPM-SDEM and MPM-LSDEM reveals that MPM-SDEM provides an enhanced efficiency and accuracy compared with the existing MPM-LSDEM method, by increases of 97% and 63%, respectively.

The calibrated MPM-SDEM model is then used to study the dynamic impact of flow-type landslide on the block by systematically varying initial column height and initial block-to-column distance. Distinct mechanisms of complete and partial submersion are identified for the block, exhibiting the differences in term of impact forces and travelling distances. Results reveal a strong positive dependence of the normalized impact force $F_{\mathrm{peak}}/F_{\mathrm{static}}$ on the Froude number Fr ($v_{\mathrm{f}}/\sqrt{gh_{\mathrm{f}}}$). Block travelling distance is governed by submersion state and exhibits strong linear correlations with the modified Froude number Fr_1 ($v_{\mathrm{f}}/\sqrt{g\mathrm{L}_0}$) for both complete and partial submersion cases. These universal scaling laws provide a quantitative basis for predicting flow-type landslide-block interactions and are believed to be helpful for landslide mitigation.

Overall, the MPM-SDEM method provides a powerful tool for enhancing landslide risk assessment and optimizing emergency response strategies through precise predictions of buried object travelling distances. Future extensions should incorporate polydisperse granular mixtures and fluid phases to better simulate real geophysical flows.

CRediT authorship contribution statement

Jun Fang: Writing – review & editing, Writing – original draft, Visualization, Methodology, Investigation, Formal analysis, Conceptualization. **Wei Ji:** Writing-original draft, Visualization, Methodology, Investigation, Formal analysis. **Tianju Xue:** Writing-review & editing, Funding acquistion. **Yu Wang:** Writing-original draft, Visualization, Methodology, Investigation, Formal analysis. **Jidong Zhao:** Writing-review & editing, Funding acquistion. **Yupeng Jiang:** Writing-review & editing, Methodology. **Clarence Edward Choi:** Writing – review & editing, Supervision, Resources, Project administration, Funding acquisition, Conceptualization.

Declaration of competing interest

The authors declare that they have no known competing financial interests or personal relationships that could have appeared to influence the work reported in this paper.

Acknowledgment

The paper acknowledges the financial support obtained from Collaborative Research Fund (C7085-24G) of the Research Grants Council of Hong Kong.

Appendix A:. Boundary condition

The boundary of the computational domain, denoted as Γ_{D}, is prescribed with a velocity $\mathbf{v}_{\mathrm{D}}$. which is dynamically determined by the combined constraint of the no-penetration and Coulomb friction. The velocity can be decomposed into normal and tangential components:

$$v_n = \mathbf{v}_{\mathrm{D}} \cdot \mathbf{n} \tag{A.1}$$

$$\mathbf{v}_t = \mathbf{v}_{\mathrm{D}} - v_n \mathbf{n} \tag{A.2}$$

where v_n is the normal velocity, $\mathbf{n}$ is the outward-pointing normal vector and $\mathbf{v}_t$ is the tangential velocity. The no-penetration condition enforces zero normal velocity at the boundary, thereby preventing any material from crossing it:

$$v_n = 0 \text{ on } \Gamma_c \tag{A.3}$$

The tangential velocity for frictional boundaries is evaluated according to the Coulomb friction law:

$$\mathbf{v}_t = \begin{cases} 0 & \text{if } ||\mathbf{v}_t|| \le \mu_w ||v_n|| \\ \mathbf{v}_t - \mu_w \left| v_n \right| \dfrac{\mathbf{v}_t}{||\mathbf{v}_t||} & \text{if } ||\mathbf{v}_t|| > \mu_w ||v_n|| \end{cases} \text{on } \Gamma_c \tag{A.4}$$

where μ_w is the friction coefficient of the wall.

Appendix B:. Constitutive model for flow-type landslide

In the proposed MPM-SDEM framework, the constitutive model employs a hypoelastic–plastic formulation capable of capturing dense, flowing, and gasification phases. When the material is dense ($\rho > \rho_c$, where ρ is the material density and ρ_c is the critical density), an additive decomposition of the velocity gradient into elastic and plastic parts is assumed as

$$\mathbf{L} = \mathbf{L}^e + \mathbf{L}^p, \tag{B.1}$$

where $\mathbf{L}$ is the velocity gradient, $\mathbf{L}^e$ is the elastic velocity gradient, and $\mathbf{L}^p$ is the plastic velocity gradient. The plastic part is given by $\mathbf{L}^p = \mathbf{D}^p = \mathbf{D}^p(\boldsymbol{\sigma})$ under assumptions of codirectionality and isochoric plastic deformation, where $\mathbf{D}^p$ is the plastic strain-rate tensor and $\boldsymbol{\sigma}$ is the Cauchy stress tensor.

The equivalent plastic shear strain rate $\dot{\gamma}^p$ is defined through the Drucker-Prager friction coefficient $\mu = \tau/p$, where $\tau = \sqrt{(1/2)\sigma_0 : \boldsymbol{\sigma}_0}$ is the equivalent shear stress, $p = -(1/3)\mathrm{tr}(\boldsymbol{\sigma})$ is the pressure (positive in compression), and $\boldsymbol{\sigma}_0 = \boldsymbol{\sigma} + p\mathbf{I}$ is the deviatoric stress tensor ($\mathbf{I}$ denotes the identity tensor).

The friction coefficient follows the $\mu(I)$ rheology:

$$\mu = \mu(I) = \begin{cases} \mu_s + \dfrac{\mu_2 - \mu_s}{I_0/I + 1} & \text{if } I > 0 \\ \mu \leq \mu_s & \text{if } I = 0 \end{cases} \tag{B.2}$$

where $I = \dot{\gamma}^p d/\sqrt{p/\rho_s}$ is the inertial number, d is the grain diameter, ρ_s is the solid grain density, μ_s is the static friction coefficient, μ_2 is the limiting dynamic friction coefficient, and I_0 is a transitional parameter. This rheology is rewritten as a rate-dependent form for the equivalent shear stress:

$$\tau = \tau(p, \dot{\gamma}^p) = \begin{cases} p\left(\mu_s + \dfrac{\mu_2 - \mu_s}{\xi\sqrt{p}/\dot{\gamma}^p + 1}\right) & \text{if } \dot{\gamma}^p > 0, \\ \tau \leq p\mu_s & \text{if } \dot{\gamma}^p = 0, \end{cases} \tag{B.3}$$

where $\xi = I_0/(d\sqrt{\rho_s/p})$ is a rate parameter (adjusted for dimensional consistency).

The stress evolution is governed by the Jaumann objective rate:

$$\dot{\boldsymbol{\sigma}} = \mathbb{C} : (\mathbf{D} - \mathbf{D}^p) + \mathbf{W}\cdot\boldsymbol{\sigma} - \boldsymbol{\sigma}\cdot\mathbf{W}, \tag{B.4}$$

where $\dot{\boldsymbol{\sigma}}$ is the objective stress rate, $\mathbb{C}$ is the fourth-order elastic stiffness tensor (depending on Young's modulus E and Poisson's ratio ν), $\mathbf{D}$ is the strain-rate tensor, and $\mathbf{W}$ is the spin tensor. When $\rho < \rho_c$, the material is considered disconnected and $\boldsymbol{\sigma} = 0$.

For numerical integration in the dense regime, a trial stress is computed assuming elastic deformation:

$$\boldsymbol{\sigma}^{\mathrm{tr}} = \boldsymbol{\sigma}^n + \Delta t\, \mathbb{C} : \mathbf{D}^{n+1} + \mathbf{W}^{n+1}\cdot\boldsymbol{\sigma}^n - \boldsymbol{\sigma}^n\cdot\mathbf{W}^{n+1}, \tag{B.5}$$

where $\boldsymbol{\sigma}^{\mathrm{tr}}$ is the trial stress tensor, Δt is the timestep. This yields trial invariants $p^{\mathrm{tr}} = -(1/3)\mathrm{tr}(\boldsymbol{\sigma}^{\mathrm{tr}})$ and $\tau^{\mathrm{tr}} = \sqrt{(1/2)\boldsymbol{\sigma}_0^{\mathrm{tr}} : \boldsymbol{\sigma}_0^{\mathrm{tr}}}$, where $\boldsymbol{\sigma}_0^{\mathrm{tr}} = \boldsymbol{\sigma}^{\mathrm{tr}} + p^{\mathrm{tr}}\mathbf{I}$ is the trial deviatoric stress tensor.

If $p^{\mathrm{tr}} \leq 0$ or $\rho^{n+1} < \rho_c$, $\boldsymbol{\sigma}^{n+1} = 0$ is set. Otherwise, the yield function $f = \tau^{\mathrm{tr}} - \mu p^{\mathrm{tr}}$ is evaluated.

If $f \leq 0$, the response is elastic:

$$\boldsymbol{\sigma}^{n+1} = \boldsymbol{\sigma}^{\mathrm{tr}}, \tag{B.6}$$

If $f > 0$, consistency is enforced by an implicit return mapping. Auxiliary parameters are defined as:

$$\begin{aligned} S_0 &= \mu_s p^{\mathrm{tr}}, \\ S_2 &= \mu_2 p^{\mathrm{tr}}, \\ \alpha_1 &= \xi G \Delta t / p^{\mathrm{tr}}, \\ B &= S_2 + \tau^{\mathrm{tr}} + \alpha_1, \\ H &= S_2 \tau^{\mathrm{tr}} + S_0 \alpha_1, \end{aligned} \tag{B.7}$$

where $G = E/(2(1+\nu))$ is the shear modulus. The quadratic equation for the updated shear stress is solved:

$$(\tau^{n+1})^2 - B\tau^{n+1} + H = 0, \tag{B.8}$$

with the root selected as:

$$\tau^{n+1} = \frac{2H}{B + \sqrt{B^2 - 4H}}, \tag{B.9}$$

The plastic shear rate is recovered as:

$$\dot{\gamma}^{p} = \frac{\tau^{\mathrm{tr}} - \tau^{n+1}}{G\Delta t}, \tag{B.10}$$

The stress is updated as:

$$\boldsymbol{\sigma}^{n+1} = \left(\frac{\tau^{n+1}}{\tau^{\mathrm{tr}}}\right)\boldsymbol{\sigma}^{0\ \mathrm{tr}} - p^{\mathrm{tr}}\mathbf{I} \tag{B.11}$$

Numerical stability and smooth phase transitions are ensured by this scheme (Dunatunga & Kamrin, 2015).

Appendix C:. Workflow of genetic algorithm

A detailed description of the genetic algorithm (GA) calibration process (Liang et al., 2023) can be concluded as follows:

(1) Initialization: An initial population of parameter sets was generated based on a combination of measured values from similar studies.. The basal friction coefficient of particles was assigned within the range [0.01, 0.5], and the maximum dynamic friction coefficient was set within the range [0.3, 0.8].
(2) Evaluation: The performance of every parameter set was assessed using a loss function that quantifies the discrepancy between the simulated block displacement and the experimental measurements.
(3) Iteration and Termination: Iterations are conducted until a target threshold of loss function is achieved or until the iteration number reaches the limit.

Appendix D:. Sensitivity analysis about the sphere radius in SDEM particle

The sphere radius is a critical parameter in generating SDEM particles, as it directly influences the contact mechanics and, consequently, the impact forces acting on the SDEM particles (Eq. (10). While adopting a smaller sphere radius improves geometric approximation of the block, it requires a smaller timestep to enforce the non-penetration constraint, thereby significantly increasing computational cost. In contrast, a larger sphere is used to generate the SDEM particle, which deviates substantially from the true block, posing challenges in accurately predicting impact force and its travelling distance. To quantify these effects, the influence of sphere radius on the accuracy of the MPM-SDEM model is systematically investigated. The additional simulations, with a timestep of 5×10^{-6} s, are conducted considering two side lengths of block ($h_{\mathrm{b}} = 20$ mm and 40 mm) and six size ratios (ranging from 1/200 to 1/8). Size ratio is defined as the ratio of sphere radius and the side length of the block.

Fig. A1 shows the effect of size ratio on the computed travelling distance of the block. For a block with a side length of 20 mm, it can be seen that the computed travelling distance is controlled by the adopted size ratio, achieving the closest prediction to experimental measurements when the size ratio is 1/20. Deviations from this optimal value significantly amplify the discrepancy between measured and computed travelling distances, with a maximum difference of 5.3% recorded. A relatively broad optimal window is observed between 1/50 to 1/10. The travelling distance for a block with a side length of 40 mm is also presented. Although experimental data is unavailable for validation, the simulations similarly reveal a strong dependence of traveling distance on size ratio, underscoring its critical role in model accuracy. Overall, a sphere-to-block size ratio of 1/20 is recommended here to balance the computational accuracy and computational cost. It is worthwhile to mention that the optimal ratio is problem-dependent. For example, finer-scale dynamic simulations involving rapid deformations typically require a smaller sphere-to-block size ratio.

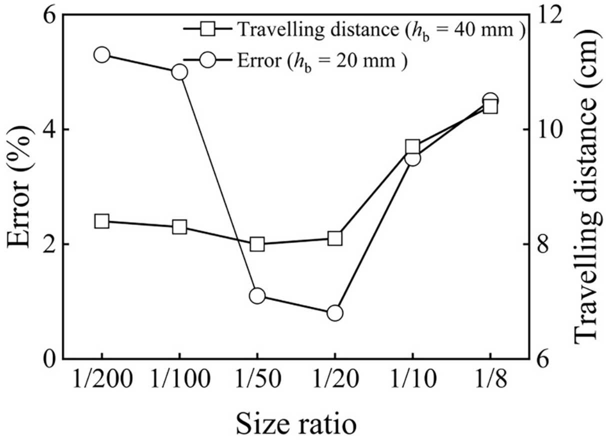

Fig. A1. The effect of the size ratio on the computed travelling distance

Data availability

Data will be made available on request.

References

Acosta, J.L.G., Vardon, P.J., Hicks, M.A., 2021. Development of an implicit contact technique for the material point method. Comput. Geotech. 130, 103859. https://doi.org/10.1016/j.compgeo.2020.103859.

Angelidakis, V., Nadimi, S., Otsubo, M., Utili, S., 2021. Clump: a code library to generate universal multi-sphere particles. SoftwareX 15, 100735. https://doi.org/10.1016/j.softx.2021.100735.

Augarde, C.E., Lee, S.J., Loukidis, D., 2021. Numerical modelling of large deformation problems in geotechnical engineering: a state-of-the-art review. Soils Found. 61 (6), 1718–1735. https://doi.org/10.1016/j.sandf.2021.08.007.

Berry, N., Zhang, Y., Haeri, S., 2023. Contact models for the multi-sphere discrete element method. Powder Technol. 416, 118209. https://doi.org/10.1016/j.powtec.2022.118209.

Bird, R.E., Pretti, G., Coombs, W.M., Augarde, C.E., Sharif, Y.U., Brown, M.J., Johnson, K., 2025. A dynamic implicit 3D material point-to-rigid body contact approach for large deformation analysis. Int. J. Numer. Meth. Eng. 126 (14), e70080. https://doi.org/10.1002/nme.70080.

Blatny, L., Baumgarten, A.S., Jop, P., 2025. Matter (v1): an open-source MPM solver for granular matter. Geosci. Model Dev. 18 (18), 9149–9171. https://doi.org/10.5194/gmd-18-9149-2025.

Caccamo, P., Chanut, B., Faug, T., Bellot, H., Naaim-Bouvet, F., 2012. Small-scale tests to investigate the dynamics of finite-sized dry granular avalanches and forces on a wall-like obstacle. Granul. Matter 14 (5), 577–587. https://doi.org/10.1007/s10035-012-0358-8.

Choi, C.E., Cui, Y., Liu, L.H.D., Ng, C.W.W., Lourenço, S.D.N., 2017. Impact mechanisms of granular flow against curved barriers. Géotech. Lett. 7 (4), 330–338. https://doi.org/10.1680/jgele.17.00068.

Choi, C.E., 2024. The 3rd Hutchinson lecture: numerical modelling of forests with uprooting as a nature-based solution to mitigate flow-type landslides. Landslides 22, 2883–2896. https://doi.org/10.1007/s10346-024-02388-5.

Cúñez, F.D., Patel, D., Glade, R.C., 2024. How particle shape affects granular segregation in industrial and geophysical flows. PNAS 121, e2307061121. https://doi.org/10.1073/pnas.2307061121.

Dai, Z., Huang, Y., Cheng, H., Xu, Q., 2017. SPH model for fluid–structure interaction and its application to debris flow impact estimation. Landslides 14, 917–928. https://doi.org/10.1007/s10346-016-0777-4.

de Vaucorbeil, A., Nguyen, V.P., Sinaie, S., Wu, J.Y., 2020a. Material point method after 25 years: theory, implementation, and applications. Adv. Appl. Mech. 53, 185–398. https://doi.org/10.1016/bs.aams.2019.11.001.

Descantes, Y., Tricoire, F., Richard, P., 2019. Classical contact detection algorithms for 3D DEM simulations: drawbacks and solutions. Comput. Geotech. 114, 103134. https://doi.org/10.1016/j.compgeo.2019.103134.

Donev, A., Torquato, S., Stillinger, F.H., 2005. Neighbor list collision-driven molecular dynamics simulation for nonspherical hard particles. I. Algorithmic details. J. Comput. Phys. 202, 737–764. https://doi.org/10.1016/j.jcp.2004.08.014.

Dunatunga, S., Kamrin, K., 2015. Continuum modelling and simulation of granular flows through their many phases. J. Fluid Mech. 779, 483–513. https://doi.org/10.1017/jfm.2015.383.

Fang, C., Gong, J., Nie, Z., Li, B., Li, X., 2021. DEM study on the microscale and macroscale shear behaviours of granular materials with breakable and irregularly shaped particles. Comput. Geotech. 137, 104271. https://doi.org/10.1016/j.compgeo.2021.104271.

Fang, J., Cui, Y., Liu, H., Zhang, L., Zhou, G.G., Fan, H., 2023. Influences of deposition upslope the barrier on the dynamic impact of dry granular flow. Eng. Geol. 323, 107212. https://doi.org/10.1016/j.enggeo.2023.107212.

Fang, J., Wang, L., Hong, Y., Zhao, J., 2022. Influence of solid–fluid interaction on impact dynamics against rigid barrier: CFD–DEM modelling. Géotechnique 72, 391–406. https://doi.org/10.1680/jgeot.19.P.160.

Faug, T., 2015. Macroscopic force experienced by extended objects in granular flows over a very broad Froude-number range: macroscopic granular force on extended object. Eur. Phys. J. E 38, 34. https://doi.org/10.1140/epje/i2015-15034-3.

Feldfogel, S., Karapiperis, K., Andrade, J., Kammer, D.S., 2024. A discretization-convergent level-set-discrete-element-method using a continuum-based contact formulation. Int. J. Numer. Meth. Eng. 125 (5), e7400.

Galindo-Torres, S.A., Pedroso, D.M., 2010. Molecular dynamics simulations of complex-shaped particles using Voronoi-based spheropolyhedra. Phys. Rev. E—Statistical, Nonlinear, and Soft Matter Physics 81 (6), 061303. https://doi.org/10.1103/PhysRevE.81.061303.

Galindo-Torres, S.A., 2013. A coupled discrete element lattice Boltzmann method for the simulation of fluid–solid interaction with particles of general shapes. Comput. Methods Appl. Mech. Eng. 265, 107–119. https://doi.org/10.1016/j.cma.2013.06.004.

Giannis, K., Kwade, A., Finke, J.H., Schilde, C., 2023. The effect of particle shape on the compaction of realistic non-spherical particles—a multi-contact dem study. Pharmaceutics 15, 909. https://doi.org/10.3390/pharmaceutics15030909.

Holtzman, R., Silin, D.B., Patzek, T.W., 2009. Mechanical properties of granular materials: a variational approach to grain-scale simulations. Int. J. Numer. Anal. Meth. Geomech. 33 (3), 391–404. https://doi.org/10.1002/nag.725.

Hu, Y., 2018. Taichi: an open-source computer graphics library. arXiv preprint arXiv: 1804.09293. DOI: 10.48550/arXiv.1804.09293.

Hungr, O., Morgan, G.C., Kellerhals, R., 1984. Quantitative analysis of debris torrent hazards for design of remedial measures. Can. Geotech. J. 21, 663–677. https://doi.org/10.1139/t84-073.

Höhner, D., Wirtz, S., Scherer, V., 2014. A study on the influence of particle shape and shape approximation on particle mechanics in a rotating drum using the discrete element method. Powder Technol. 253, 256–265. https://doi.org/10.1016/j.powtec.2013.11.023.

Hübl, J., Suda, J., Proske, D., Kaitna, R., Scheidl, C., 2009. Debris flow impact estimation. In Proceedings of the 11th international symposium on water management and hydraulic engineering, Ohrid, Macedonia (Vol. 1, pp. 1–5). University of Ss Cyril and Methodius, Faculty of Civil Engineering, Skopje, Macedonia.

Iverson, R.M., George, D.L., 2014. A depth-averaged debris-flow model that includes the effects of evolving dilatancy. I. Physical basis. Proc. R. Soc. A 470, 20130819. https://doi.org/10.1098/rspa.2013.0819.

Jiang, C., Schroeder, C., Teran, J., Stomakhin, A., Selle, A., 2016. The material point method for simulating continuum materials, in: ACM SIGGRAPH 2016 Courses. ACM, New York, pp. 1–52. DOI: 10.1145/2897826.2927348.

Jiang, Y., Zhao, Y., Choi, C.E., Choo, J., 2022. Hybrid continuum–discrete simulation of granular impact dynamics. Acta Geotech. 17, 5597–5612. https://doi.org/10.1007/s11440-022-01598-2.

Jiang, Y., Li, M., Jiang, C., Alonso-Marroquin, F., 2020. A hybrid material-point spheropolygon-element method for solid and granular material interaction. Int. J. Numer. Meth. Eng. 121, 3021–3047. https://doi.org/10.1002/nme.6345.

Jóhannesson, T., Gauer, P., Issler, P., Lied, K., Hákonardóttir, K.M., 2009. The design of avalanche protection dams: recent practical and theoretical developments. European Commission, Belgium. https://doi.org/10.3189/002214309789470888.

Kim, J., Kim, H.J., Park, H.J., 2025. Comparative analysis of granular material flow: discrete element method and smoothed particle hydrodynamics approaches. Phys. Fluids 37 (5). https://doi.org/10.1063/5.0268155.

Lagmay, A.M.A., Tengonciang, A.M.P., Rodolfo, R.S., Soria, J.L.A., Baliatan, E.G., Paguican, E.R., Uichanco, C.L., 2008. Science guides search and rescue after the 2006 Philippine landslide. Disasters 32 (3), 416–433. https://doi.org/10.1111/j.1467-7717.2008.01047.x.

Lai, Z., Zhao, J., Zhao, S., Huang, L., 2023. Signed distance field enhanced fully resolved cfd-dem for simulation of granular flows involving multiphase fluids and irregularly shaped particles. Comput. Methods Appl. Mech. Eng. 414, 116195. https://doi.org/10.1016/j.cma.2023.116195.

Liang, Z., Choi, C.E., Zhao, Y., Jiang, Y., Choo, J., 2023. Revealing the role of forests in the mobility of geophysical flows. Comput. Geotech. 155, 105194. https://doi.org/10.1016/j.compgeo.2022.105194.

Liu, B., Wang, W., Liu, Z., Ouyang, N., Mao, K., Zhou, F., 2024. Study on large deformation of soil–rock mixed slope based on gpu accelerated material point method. Sci. Rep. 14, 6983. https://doi.org/10.1038/s41598-024-57362-x.

Liu, B., Cen, W., Yan, G., Scheuermann, A., Zheng, C., Zhang, P., 2025. Particle shape effects on breakage behaviors in granular materials: a multiscale geotechnical perspective. Comput. Geotech. 187, 107504. https://doi.org/10.1016/j.compgeo.2025.107504.

Liu, C., Sun, Q., Zhou, G.G.D., 2018. Coupling of material point method and discrete element method for granular flows impacting simulations. Int. J. Numer. Meth. Eng. 115 (2), 172–188. https://doi.org/10.1002/nme.5800.

Ng, C.W.W., Wang, C., Choi, C.E., De Silva, W.A.R.K., Poudyal, S., 2020. Effects of barrier deformability on load reduction and energy dissipation of granular flow impact. Comput. Geotech. 121, 103445. https://doi.org/10.1016/j.compgeo.2020.103445.

Ng, C.W.W., Majeed, U., Choi, C.E., De Silva, W.A.R.K., 2021. New impact equation using barrier Froude number for the design of dual rigid barriers against debris flows. Landslides 18 (6), 2309–2321. https://doi.org/10.1007/s10346-021-01631-7.

Poudyal, S., Choi, C.E., Song, D., Zhou, G.G.D., Yune, C.Y., Cui, Y., Leonardi, A., Busslinger, M., Wendeler, C., Pition, G., Moase, E., Strouth, A., 2019. Review of the mechanisms of debris-flow impact against barriers. In Association of Environmental and Engineering Geologists; Colorado School of Mines. Arthur Lakes Library. Special publication 28, 1027–1304.

Qu, T., Feng, Y.T., Zhao, T., Wang, M., 2019. Calibration of linear contact stiffnesses in discrete element models using a hybrid analytical-computational framework. Powder Technol. 356, 795–807. https://doi.org/10.1016/j.powtec.2019.09.016.

Ren, S., Zhang, P., Galindo-Torres, S.A., 2022. A coupled discrete element material point method for fluid–solid–particle interactions with large deformations. Comput. Methods Appl. Mech. Eng. 395, 115023. https://doi.org/10.1016/j.cma.2022.115023.

Salciarini, D., Tamagnini, C., Conversini, P., 2010. Discrete element modeling of debris-avalanche impact on earthfill barriers. Phys. Chem. Earth 35, 172–181. https://doi.org/10.1016/j.pce.2009.05.002.

Shi, Y.H., Guo, N., Yang, Z.X., 2024. Geotaichi: a taichi-powered high-performance numerical simulator for multiscale geophysical problems. Comput. Phys. Commun. 301, 109219. https://doi.org/10.1016/j.cpc.2024.109219.

Song, D., Bai, Y., Chen, X.Q., Zhou, G.G., Choi, C.E., Pasuto, A., Peng, P., 2022. Assessment of debris flow multiple-surge load model based on the physical process of debris-barrier interaction. Landslides 19, 1165–1177. https://doi.org/10.1007/s10346-021-01778-3.

Song, D., Ng, C.W.W., Choi, C.E., Kwan, J.S.H., Koo, R.C.H., 2017. Influence of debris flow solid fraction on rigid barrier impact. Can. Geotech. J. 54 (10), 1421–1434. https://doi.org/10.1139/cgj-2016-0502.

Stomakhin, A., Schroeder, C., Chai, L., Teran, J., Selle, A., 2013. A material point method for snow simulation. ACM Trans. Graph. 32 (4), 1–10. https://doi.org/10.1145/2461912.2461948.

Su, Y., Cui, Y., Ng, C.W.W., Choi, C.E., Kwan, J.S.H., 2019. Effects of particle size and cushioning thickness on the performance of rock-filled gabions used in protection against boulder impact. Can. Geotech. J. 56, 198–207. https://doi.org/10.1139/cgj-2017-0370.

Sveinsson, H.A., Hafreager, A., Kalia, R.K., Nakano, A., Vashishta, P., Malthe-Sørenssen, A., 2020. Direct atomic simulations of facet formation and equilibrium shapes of SiC nanoparticles. Cryst. Growth Des. 20, 2147–2152. https://doi.org/10.1021/acs.cgd.9b00612.

Thibert, E., Baroudi, D., Limam, A., Berthet-Rambaud, P., 2008. Avalanche impact pressure on an instrumented structure. Cold Reg. Sci. Technol. 54, 206–215. https://doi.org/10.1016/j.coldregions.2008.01.005.

Troncone, A., Pugliese, L., Parise, A., Mazzuca, P., Conte, E., 2025. Post-failure stage analysis of flow-type landslides using different numerical techniques. Comput. Geotech. 182, 107152. https://doi.org/10.1016/j.compgeo.2025.107152.

Trujillo-Vela, M.G., Galindo-Torres, S.A., Zhang, X., Ramos-Cañón, A.M., Escobar-Vargas, J.A., 2020. Smooth particle hydrodynamics and discrete element method coupling scheme for the simulation of debris flows. Comput. Geotech. 125, 103669. https://doi.org/10.1016/j.compgeo.2020.103669.

Wang, M., Kumar, K., Feng, Y.T., Qu, T., Wang, M., 2025a. Machine learning aided modeling of granular materials: a review. Arch. Comput. Meth. Eng. 32, 1997–2034. https://doi.org/10.1007/s11831-024-10199-z.

Yu, X., Li, W., Zhang, G., 2024. Research on the distribution of debris flow impact on the upstream surface of the check dam. Sci. Rep. 14, 25281. https://doi.org/10.1038/s41598-024-76558-9.

Zhang, J., Yang, M., Li, X., Jiang, Q.O., Zhang, H., Meng, W., 2024. Two-particle debris flow simulation based on SPH. Comput. Animat. Virtual Worlds 35, e2261.

Zhao, T., Crosta, G.B., Utili, S., De Blasio, F.V., 2017. Investigation of rock fragmentation during rockfalls and rock avalanches via 3D discrete element analyses. J. Geophys. Res. Earth Surf. 122, 678–695. https://doi.org/10.1002/2016JF004060Digital Object Identifier (DOI).

Zhao, W., Wang, R., Liu, X., Ju, N., Xie, M., 2020. Field survey of a catastrophic high-speed long-runout landslide in Jichang Town, Shuicheng County, Guizhou, China, on July 23, 2019. Landslides 17 (6), 1415–1427. https://doi.org/10.1007/s10346-020-01380-z.

Zhao, Y., Choo, J., Jiang, Y., Li, M., Jiang, C., Soga, K., 2022. A barrier method for frictional contact on embedded interfaces. Comput. Methods Appl. Mech. Eng. 393, 114820. https://doi.org/10.1016/j.cma.2022.114820.

Zhou, Y., Shi, Z., Zhang, Q., Liu, W., Peng, M., Wu, C., 2019. 3D DEM investigation on the morphology and structure of landslide dams formed by dry granular flows. Eng. Geol. 258, 105151. https://doi.org/10.1016/j.enggeo.2019.105151.